Combined Sentinel-1 and - 2 soil moisture retrieval for a corn and wheat field in Twente

ZHOOBIN RAHIMI
JULY, 2020

SUPERVISORS:
dr. ir. Rogier van der velde
dr. ir. Suhyb Salama

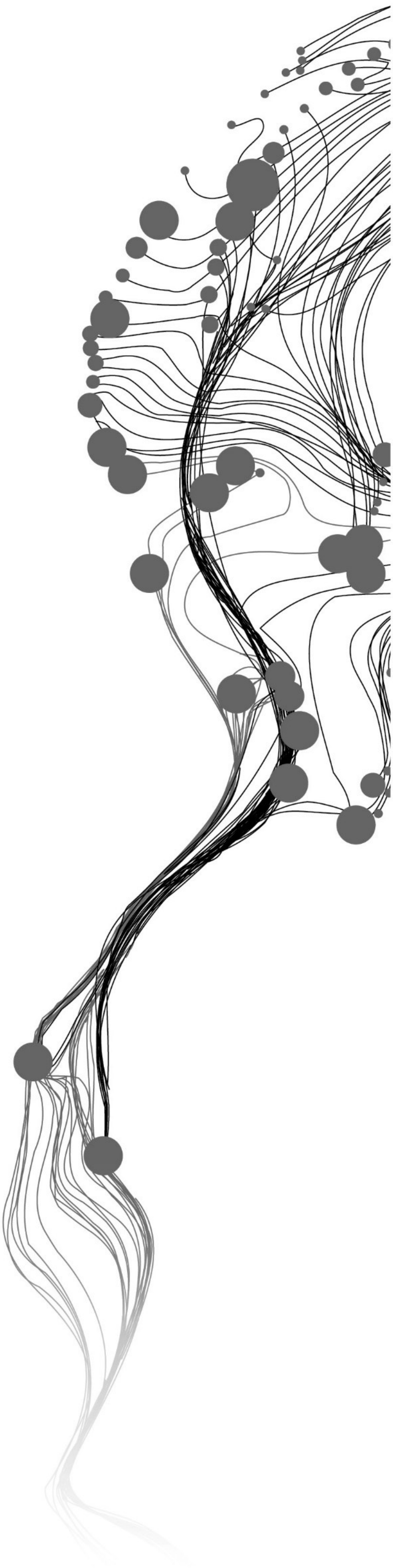

Combined Sentinel-1 and - 2 soil moisture retrieval for a corn and wheat field in Twente region

ZHOOBIN RAHIMI
Enschede, The Netherlands, [July, 2020]

Thesis submitted to the Faculty of Geo-Information Science and Earth Observation of the University of Twente in partial fulfilment of the requirements for the degree of Master of Science in Geo-information Science and Earth Observation.
Specialization: Water resource and environmental management

SUPERVISORS:
Dr. Ir. Rogier van der Velde
Dr. Ir. Suhyb Salama

THESIS ASSESSMENT BOARD:
Prof. Dr. Z. Bob Su (Chair)
Dr. D.C.M. Augustijn (External Examiner, ET-WEM University of Twente)

ABSTRACT

There is an escalating interest for water to inundate farming fields and to keep up groundwater levels, particularly in dry periods. It has been indicated that when there is a lack of knowledge about the soil moisture, the water usage for rural water supply excessively increases. As a result, a soil moisture-based water system is an efficient approach to improve water resource management. This study improved and assessed a remote sensing-based approach to retrieve soil moisture via a combined Sentinel-1 and Sentinel -2 dataset in the Twente region, the Netherlands. Two crop types, such as wheat and corn, were selected as they are two of the most important agricultural products that were planted and rotated in the study area. Two primary sources of satellite data, including Sentinel-1 C- band and Sentinel-2, were collected and processed via Google Earth Engine to ease the data collection and processing. The soil moisture retrieval algorithm that was developed for this study is based on integrating a calibrated Integral Equation Model (IEM) with a modified water cloud model (WCM) to remove the effects of vegetation. The IEM was mostly affected by the attenuation process at the wheat field. At the same time, it was mostly dominated by the scattering process through the cornfield. The modified WCM significantly removes the vegetation effect. The validation process was carried out for wheat and corn at 50, and 90 m aggregated subsets, respectively. The temporal variation of retrieved soil moisture in the wheat field was not fully understood as the RMSE error was widely different, between 0.09 and 0.2 [m3/m3] for ascending and descending C-band backscattering observations, respectively. However, the scene-based validation at 12.5 m spatial resolution shows consistency accuracy within the study area.

ACKNOWLEDGMENTS

I would like to thank both of my supervisors, Dr. Ir. Rogier van der Velde and Dr. Suhyb Salama very much for the patient guidance, encouragement, and advice they have provided for me during my time as their student. I have been fortunate to have supervisors who cared so much about my work, and who responded to my questions and queries so promptly. In fact, being their student was one of my greatest experiences I ever had, and I will miss every single time that we seated together and discussed.

I must express my gratitude to my parents for their continued support and encouragement. I was continually amazed by the patience of my mother, and father who experienced all of the ups and downs of my life and my study.

Finally, I would like to thank the Faculty of Geo-Information Science and Earth Observation (ITC), not only for providing the funding which allowed me to undertake this program but also for giving me the opportunity to learn so much knowledge and meet so many lovely people. It has always been one of my dreams that came true!

TABLE OF CONTENTS

1. Introduction 7

1.1. Background 7

1.2. Literature Review 8

1.3. Research Problem 9

1.4. Research Objectives and Questions 9

1.5. Conceptual framework of research: 10

2. Study area and field measurements 12

2.1. Twente region 12

2.2. Twente regional network 12

2.3. LoRa soil moisture network 12

2.4. Soil moisture monitoring networks instrumentation 14

2.5. Ancillary data 14

3. Remote Sensing data 16

3.1. Sentinel-1 A/B 16

3.2. Sentinel-2 A/B 16

3.3. Data access via Google Earth Engine 17

4. Methods 18

4.1. Normalized Differential Vegetation Index (NDVI) 18

4.2. Integrating the Water Cloud model with IEM 18

4.3. Retrieving soil moisture via inverse WCM 19

4.4. Root mean square error 19

4.5. Pearson correlation coefficient (r) 19

5. Results and discussion 20

5.1. Spatial and temporal matching 20

5.2. Calibration and validation of roughness parameters for the wheat field 25

5.3. Calibration and validation of roughness parameters for the cornfield 32

5.4. Normalized Differential Vegetation Index (NDVI) 34

5.5. Assessment of Harmonic Analysis of Time Series (HANTS) for NDVI 36

5.6. Optimizing crop factors for winter wheat 37

5.7. Optimizing crop factors for Cornfield 39

5.8. Effect of Surface Parameters on Backscattering observations in IEM 43

5.9. Retrieving soil moisture 43

6. Implementation of GEE-based soil moisture retrieval (SMR) platform 49

6.1. Introduction 49

6.2. Technical Requirments 49

6.3. Running SMR 50

6.4. Python installation and processing 53

6.5. SMR output 56

7. Conclusion 60

LIST OF FIGURES

Figure 1 the conceptual framework of this study.......11
Figure 2 map of monitoring stations known as the Twente network located in the east of the Netherlands.......12
Figure 3 (a) Soil moisture measuring network known as LoRa network during the winter of 2017, (b) Installation of two extra LoRa units close to the soil moisture station at ITCSM10 on 2018/02/02. (c) The situation of fields and the soil moisture stations at ITCSM10 on 2018/07/11.......13
Figure 4 The air temperature data at 10 cm above the surface collected from the weather station in Twente airport.......14
Figure 5 Landcover map for the Netherlands (https://www.clo.nl/node/20807).......15
Figure 6 Decision tree of cloud filtering.......17
Figure 7 present the spectral bands of sentinel-2---cite.......18
Figure 8 correlation between soil moisture values at ITCSM_10 and the mean of Lora based soil moisture observations at five different subsets.......21
Figure 9 Pearson correlation between soil moisture values at ITCSM_10 and backscatter values of Sentinel-1 at five different subsets.......22
Figure 10 forward correlation between soil moisture values of LoRa Stations and backscatter values of Sentinel-1 at five different subsets.......23
Figure 11 backward correlation between soil moisture values of LoRa Stations and backscatter values of Sentinel-1 at five different subsets.......23
Figure 12 Pearson Correlation values between S1 and instant values of SMC from LoRa Network.......24
Figure 12 Distribution of R and RMSE between rms height and correlation length in ascending path.......27
Figure 13 Distribution of R and RMSE between RMS height and correlation length in the descending path.......28
Figure 14. Simulated backscattering coefficients based and calibrated roughness parameters for descending observations.......29
Figure 15. Compare simulated backscattering coefficients based and calibrated roughness parameters for ascending observations.......29
Figure 16 validated backscattering coefficients based on calibrated roughness parameters for descending observations.......30
Figure 17 validated backscattering coefficients based on calibrated roughness parameters for ascending observations.......30
Figure 18 obtained validation results for April, May, June, and July, 2018 as significant vegetation growth is expected during this period for ascending path.......31
Figure 19 obtained validation results for April, May, June, and July, 2018 as significant vegetation growth is expected during this period for descending path.......32
Figure 20 Compare the daily variation of soil water content with derived NDVI from MODIS, Landsat-8, and Sentinel-2.......34
Figure 21 Compare the monthly average of NDVI products.......35
Figure 22 The images from Triple-Sat demonstrate the growing cycle of winter wheat from March to September, 2018. Source: The Netherlands Space Office (https://www.spaceoffice.nl/nl/satellietdataportaal/beschikbare-data/uitleg-data/product-levels/).......36
Figure 23 overview of estimated total backscattering value and backscattering observations for winter wheat.......38
Figure 24 compares the total backscattering value and ascending observations of Sentinel-1 in the cornfield.......41
Figure 25 compares the total backscattering value and descending observations of Sentinel-1 in the cornfield.......42

Figure 26 shows the effect of surface parameters on the backscattering coefficient in IEM for the wheat field (on the left), and cornfield 43
Figure 27 footprint of sentinel-1 backscatter observations at 50m subset via GEE along with the underlying TripleSat image captured on 5, September, 2018 44
Figure 28 footprint of Sentinel-1 backscatter observations at 10m subset via GEE along with the underlying TripleSat image captured on 5, September, 2018 44
Figure 29 footprint of sentinel-1 backscatter observations at 90m subset via GEE along with the underlying TripleSat image captured on 5, September, 2018 45
Figure 30 show the retrieved soil moisture against the soil moisture measurements for ascending and descending observations during Wheat grow cycle 47
Figure 31 show the retrieved soil moisture against the soil moisture measurements for ascending and descending observations during corn grow cycle 48
Figure 32 the design of GEE web service source 49

LIST OF TABLES

Table 1 Characteristics of Sentinel-1 Interferometric Wide Swath Instrument 16
Table 2 Characteristics of Sentinel-2 for Multi-Spectral Instrument 17
Table 3 List of stations involved to obtain the average values 20
Table 4 Statistical summary of averaged soil moisture values at five different subsets 20
Table 5 statistical summary of the correlation between the soil moisture values of ITCSM_10 and LoRa Stations at five different subsets 21
Table 6, Statistical summary of backscatter values at five different subsets 22
Table 7 statistical summary of the correlation between the soil moisture values of LoRa Stations and backscatter values of Sentinel-1 at five different subsets 24
Table 8 compares correlation values between the spatial mean of soil moisture values and the daily average 25
Table 9 Show an example of the LUT for inserting the frequency, incident angle, the roughness parameters, and dielectric constant in IEM 25
Table 10 present the dedicated validation and calibration periods for checking the optimization process . 26
Table 11 shows obtained surface roughness parameters, RMSE, and the r based on simulated Daily basis backscattering coefficients for the wheat field. 28
Table 12 obtained validation results in ascending and descending paths for April, May, June, and July 2018 31
Table 13 present the dedicated validation and calibration periods for checking the optimization process in the cornfield 32
Table 14 comparing the simulation results and observed backscattering observations at different spatial subsets 33
Table 15 comparing the IEM results and observed backscattering observations between 1st and 17th September 2018 33
Table 16 obtained validation results in ascending and descending paths in between 1st and 17th September 2018 33
Table 17 The estimated values of crop factor for winter wheat on April, May, June, and July, 2018 37
Table 18 shows the estimated values of crop factor for ascending observations of Sentinel-1 in a cornfield 39
Table 19 The estimated values of crop factor for descending observations of Sentinel-1 in corn field 40
Table 20 list of collected images for validation of retrieved soil moisture during the wheat growing cycle via GEE 45
Table 21 show the accuracy of Scene-based retrieved soil moisture during the wheat growing cycle 46
Table 22 show the accuracy of Time series retrieved soil moisture during the wheat and corn growing cycle 46

1. INTRODUCTION

1.1. Background

Synthetic Aperture Radar (SAR) observations by Sentinel-1 C-band can be used to retrieve soil moisture. However, due to vegetation cover, uncertainties in calibration, and speckle Noise, SAR observations come with inaccuracies. Moreover, observations of Sentinel-2 in an optic range can be used to estimate vegetation cover that leads to mitigate the inaccuracy due to vegetation effect.

Agriculturally, by efficient irrigation and crop rotation, communities can make the impact of drought much less severe. Failing an adequate drought mitigation plan can deliver a severe cost to communities. As the Netherlands, as well as many other countries in western Europe, are experiencing extreme drought periods, reliable information about soil moisture, vegetation health, and water levels can help to protect, mitigate, and relieve the drought. However, providing the required data at regional and global scales is challenging. The remote sensing-based technique can provide an ironic combination of related data for drought monitoring, which is one of the most reliable and efficient solutions for this problem.

Remotely sensed soil moisture data provide the spatial and temporal information needed to improve water productivity and the efficiency of irrigation (FAO, 2018). There are several soil moisture products from microwave remote sensing satellites, including Soil moisture Ocean Salinity (SMOS) and soil moisture active passive (SMAP) with approximately ($0.25^\circ \times 0.25^\circ$) spatial resolution Entekhabi et al. (2014). These products are helping us with monitoring drought and improving agricultural productivity on a global scale (Cui et al., 2018; Martínez-Fernández, González-Zamora, Sánchez, Gumuzzio, & Herrero-Jiménez, 2016). However, monitoring soil moisture at a global scale is not so much appealing to researchers and humans as the soil moisture is highly variable in time and space. The coarse spatial resolution of SMOS, SMAP, and other non-commercial microwave satellites remains a limiting factor for monitoring soil moisture at regional and local scales. combining Sentinel-1 and sentinel-2 observations is likely to provide same revisit frequency, but enhanced spatial resolution and reliable soil moisture data which is promising to improve monitoring and assessment of drought and perhaps leading to improve agricultural productivity

Collecting data is also a challenging issue. Retrieving data from Google Earth Engine (GEE) is relatively new, and a few researches have been conducted so far. Moreover, there have been a few conducted pieces of research that use GEE to retrieve soil moisture in the past (Nyamu, 2019; Sazib, Mladenova, & Bolten, 2018). This study aims to produce high-resolution soil moisture products for improving crop management and irrigation via GEE as a data processing and data exploration platform. Since the rapid growth in crop biomass complicates the retrieval of soil moisture, a better representation of the vegetation cover is needed. This study combines Sentinel-1 and Sentinel-2 to account for the effect of crop biomass and retrieve soil moisture with higher spatial resolution and consistency. The sentinel-1 and Sentinel-2 satellites are based on a constellation of two satellites to achieve revisit and coverage requirements, which deliver vigorous datasets for researchers and scientists on the field of earth observation.

1.2. Literature Review

1.2.1. Scattering Process

The backscattering observations of C-band Sentinel-1 are sensitive to the dielectric constant; therefore, the dielectric constant can be translated to soil moisture via C-band backscattering observations (Mironov, Kosolapova, & Fomin, 2009). Currently, several models can reproduce backscattering coefficients, i.e., analytical and empirical models (Dubois, Van Zyl, & Engman, 1995; Ulaby & Long, 2014). Both models can simulate σ^0 using the given dielectric constant and roughness of the soil surface as well as the configurations of the sensor. By inverting the algorithms and comparing the simulated σ^0 with the observed σ^0, it is possible to retrieve soil moisture (Barrett, Dwyer, & Whelan, 2009).

In addition, in a densely vegetated area, i.e., during the final development stages of wheat, the vegetation significantly affects the C-band backscattering observations (Mattia et al., 2003). Knowing the biophysical parameters of vegetation can significantly help us to understand the scattering and attenuation effect of vegetation and assess the quantity of vegetation effect on backscattering observations. As a result, coupling a vegetation model that can accurately add the vegetation scattering and attenuation process to the analytical solution can deliver a robust framework to remove the vegetation effect and estimate actual soil moisture values underlying the vegetation cover. The analysis of the different model combinations within one framework can be seen as the most significant advantage of combining surface backscattering models with canopy models (Baghdadi, Hajj, Zribi, & Bousbih, 2017; Kirimi et al., 2016).

1.2.2. Integral Equation Method (IEM) surface scatter model

An incident wavelength that penetrates reflects or backscatter from the ground surface due to the physical interaction generates a backscattering coefficient (σ^0). The σ^0 can be calculated via surface backscattering models to retrieve more information about the spatial variability of water content in the open and sparsely vegetated field (Rodriguez-Alvarez et al., 2011). Surface backscattering models are divided into different categories, including analytical, e.g., Integral equation model (IEM) Fung, Li, & Chen (1992), and semi-empirical solutions (Dubois et al., 1995; Yisok; Oh, Sarabandi, & Ulaby, 1992).

IEM as an analytical solution describes the backscattering process from a physical perspective which is able to account for different sensing configurations (e.g., wavelength, polarization and incidence angle) except for the surface geometries (i.e., roughness parameters) (Aubert et al., 2011; Lievens et al., 2009; Verhoest et al., 2008). As a result, calibrating the roughness parameters to retrieve soil moisture from backscattering observation is extremely important (Bryant et al., 2007).

The IEM model is the most commonly used method to simulate backscattering coefficients in farm fields (Baghdadi et al., 2018; Kornelsen & Coulibaly, 2013), but a few weaknesses limit its performance. First, the model is limited to relate the radar backscattering coefficient to bare soil. Therefore, it is not possible to accurately simulate backscattering coefficients in a vegetated land cover (Verhoest et al., 2007). Second, the IEM model is designed based on theoretically derived equations not using in situ measurement. Therefore, the unknown values of roughness parameters introduce significant bias into the simulated backscattering coefficients.

By inverting the IEM model of simulating the backscattered coefficients and comparing simulated backscatter coefficients with actual backscatter coefficients, it is possible to retrieve the soil moisture content (SMC) from backscattering observations (Y. Oh, Sarabandi, & Ulaby, 1994).

1.2.3. Effects of dielectric properties

The dielectric variation of any surface is always affected by the texture and the water content of that surface (Dam, Borchers, Hendrickx, & Harmon, 2003; Gorrab et al., 2015; Srivastava, Patel, & Navalgund, 2006). Although the relationship between soil moisture and dielectric properties is very complicated, a linear relationship between soil moisture and dielectric constant has been determined experimentally. This has led to the development of the soil-dielectric mixing model (Dobson, et.al., 1985).

1.2.4. Vegetation effect

Most developed backscattering models are suitable for bare soil. As the vegetation grows, the interaction between vegetation and incident signal becomes extraordinarily complex, and consequently, retrieving soil moisture in vegetated terrains become more complicated (Pierdicca, Pulvirenti, & Bignami, 2010). Besides, the more interaction between vegetation and incident signal, the more uncertainty will be added to the retrieved soil moisture (Bindlish et al., 2009). Although no straight forward approach exists at present, approximate solutions are sufficient for a wide range of practical experiments(Choker et al., 2017). One solution is to use a radiative transfer model known as Water Cloud Model (WCM) developed by (Attema & Ulaby, 1978). The WCM is able to quantitatively analyze the effect of the scattering and attenuation process of vegetation. Previous studies used the Water cloud model (WCM) to investigate the behavior of backscattering coefficients in corn and wheat fields (Joseph, van der Velde, O'Neill, Lang, & Gish, 2010; Mattia et al., 2003). As a result, integrating the water cloud model with IEM help us to arrive at a better quantification of the vegetation characteristics on backscattering observations from Sentinel-1 (Hajj, Baghdadi, Zribi, & Bazzi, 2017; Kirimi et al., 2016).

1.3. Research Problem

Retrieving soil moisture from backscattering observations is always a challenging issue because the effects of the surface roughness and vegetation on backscatter observations are difficult to quantify. Particularly in farmlands, where the rapid growth in crop biomass complicates the retrieval of soil moisture even further, lack of knowledge about the dynamics of vegetation characteristics could lead to a significant bias in soil moisture retrieval from backscatter observations. This complexity is mostly related to dynamics in the scattering and attenuation characteristics of vegetation during the growth cycle. Given that the dynamic characteristics of vegetation cannot be described by the IEM model, accounting for a valid model that addresses the effects of vegetation in soil moisture retrievals is a critical problem.

1.4. Research Objectives and Questions

The main focus of this study is to improve the retrieval of soil moisture for corn and wheat via combining Sentinel-1 and Sentinel-2 data. The soil moisture retrieval algorithm that will be developed for this study is based on the IEM surface scattering model in combination with the Water cloud model (WCM) Attema & Ulaby (1978) to account for the effects of vegetation.

The sub-objectives formulated are:

- to assess the spatial and temporal match between the backscattering observation of sentinel-1 and soil moisture data,
- to analyze the effects of surface roughness on the Sentinel-1 σ^0 and calibrate roughness parameters for IEM surface scattering model,

- to analyze the effects of corn and winter wheat on the Sentinel-1 σ^0 and test suitability of WCM to correct for these vegetation effects,
- to develop a radiative transfer model for simulating σ^0 of the soil-vegetation system observed by Sentinel-1 as a basis for soil moisture retrieval algorithm,

The research questions that will be addressed in the proposed research are:

1. To what extent does the analysis of the spatial and temporal soil moisture variability, allows us to understand its relationship with the backscattering behavior of Sentinel-1?
2. What is the reliability of the surface roughness parameterization for the IEM model derived for bare soil conditions?
3. What is the main vegetation effect (i.e., scattering and attenuation process) of WCM to account for the effects of corn and wheat on Sentinel-1 σ^0?
4. What is the dominant parameter that affects the Sentinel-1 backscatters the most in corn and wheat fields?

1.5. Conceptual framework of research:

An overview of the main steps applied in this study consists of:
A first step is to find the best spatial resolution at which sentinel-1 backscattering observations and soil moisture measurements from the Lora network match the best. Comparing the correlations between soil moisture measurements from the LoRa network at different subsets will provide us more information about the behaviour of aggregated Sentinel-1 backscatter observations over different windows. It will lead us to choose the most effective resolution for soil moisture retrieval.

The second step is to estimate the surface roughness parameters (i.e., RMS height (s) and length function (l)) for IEM surface scattering model using the in-situ measurements. The ground measurements of soil moisture were separated in different periods based on vegetation cover (i.e., bare soil and vegetated soil). An accurate estimation of the roughness parameter requires to be carried out when the bare soil is dominant. As a result, the winter period between the harvesting and sowing was selected to run the IEM directly. The output is the calibrated surface roughness parameters, which will be used as an input parameter to retrieve soil moisture in the inverses model.

The third step is to investigate the effect of vegetation, which will be done by separating the vegetation growth cycles into corn and wheat periods using the water cloud model.

In the final step, the calibrated crop parameters are used in an algorithm to retrieve soil moisture, which will be validated against the in-situ measurements. Figure 1 presents an overview of the methodology of this study.

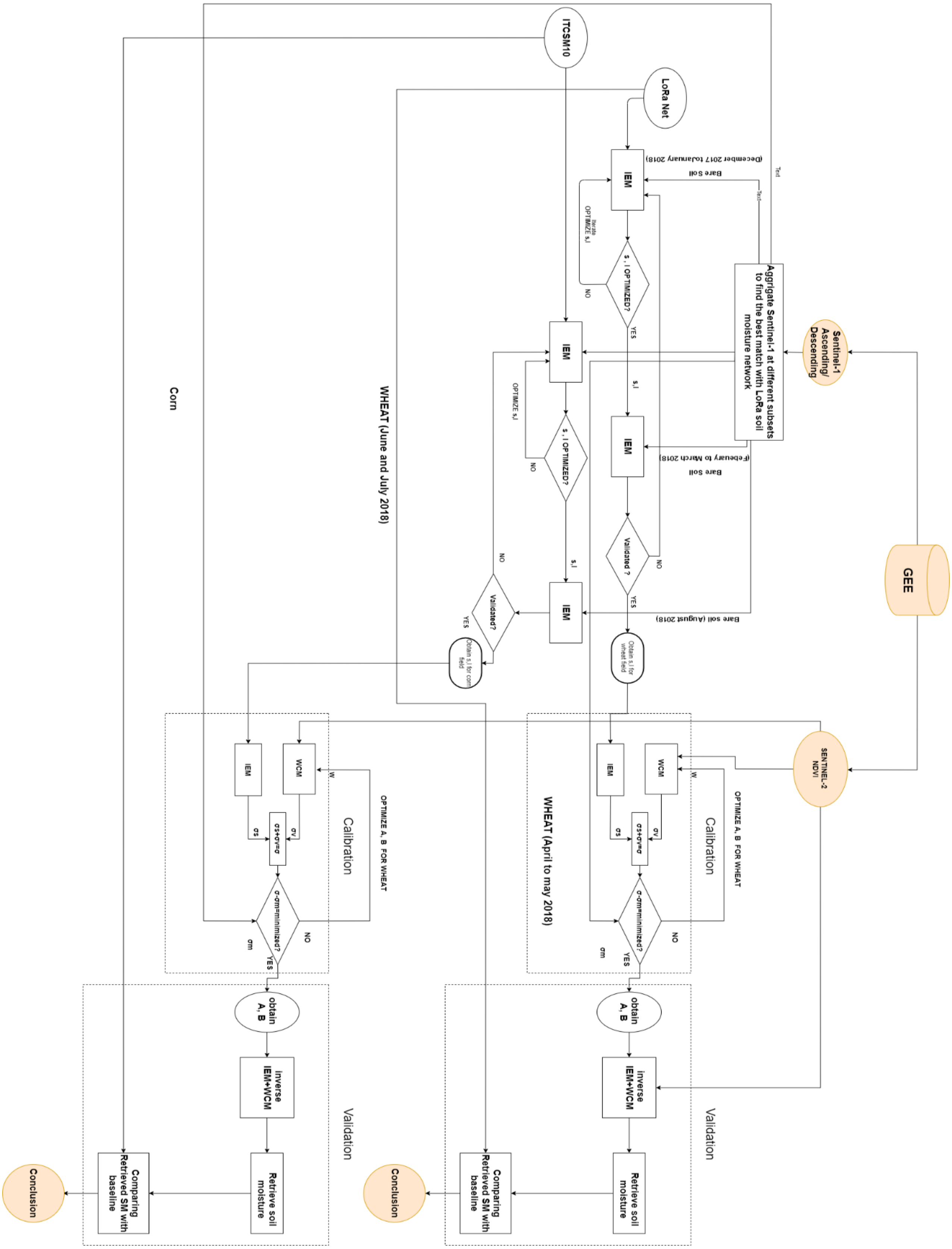

Figure 1 the conceptual framework of this study

2. STUDY AREA AND FIELD MEASUREMENTS

2.1. Twente region

Twente region is located in the Overijssel province, the eastern part of the Netherlands (52° 05'–52° 27'N and 6° 05'–7° 00'E). The elevation of the Twente region varies from -10 to 150 meters above sea level, as shown in figure 2. Over 70 percent of the land use is dedicated to farmlands in the Overijssel province (CBS, 2016). The soil type in this area consists of 95% sand and 5% clay.

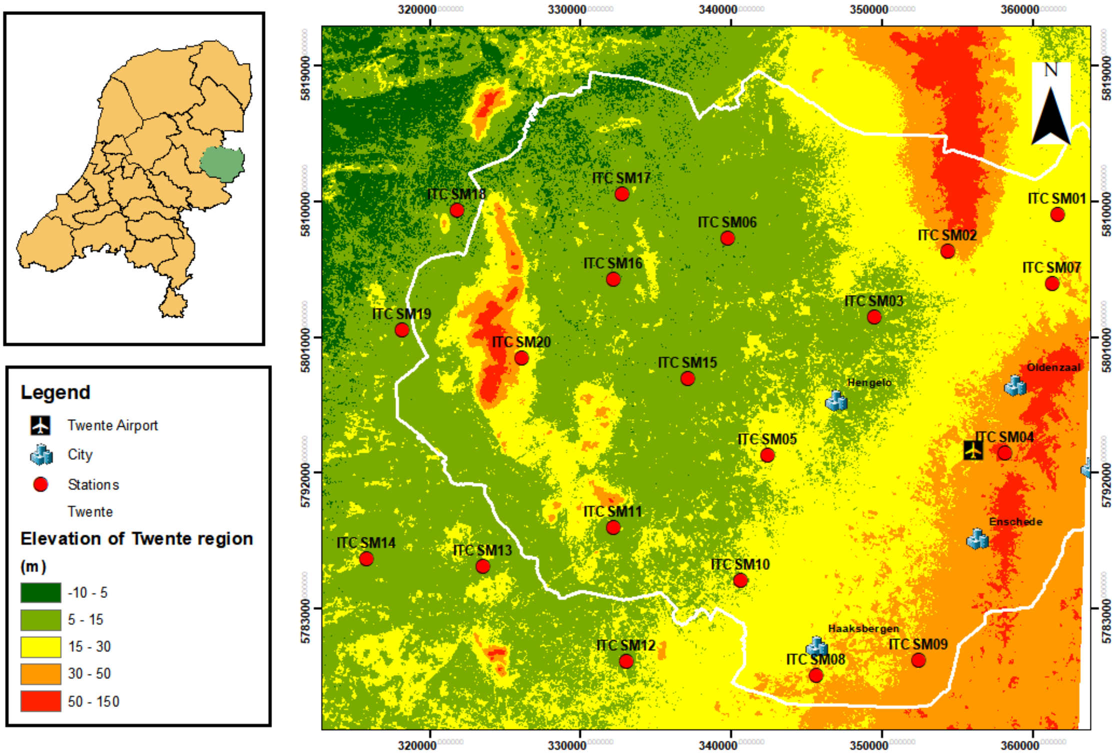

Figure 2 map of monitoring stations known as the Twente network located in the east of the Netherlands

2.2. Twente regional network

The Twente regional network consists of 20 stations is constantly collecting soil moisture data, as shown in figure 1. They have been collecting data from December 2009 up to June 2020. The Ground measurements from the soil moisture monitoring network at 40 km × 50 km area will be used for calibration and validation of retrieved soil moisture from Sentinel-1. This study focuses on station ITCSM10, which has been collecting soil moisture from 2016 until 2019. The collected soil moisture data at 5 cm represents accumulated soil moisture content from 1 cm up to a 9 cm depth below the surface.

2.3. LoRa soil moisture network

A low-power wide-area network (LPWAN) protocol known as LoRa (Long Range) network was developed to measure soil moisture. Twenty-four stations were distributed across the farmland at Hengevelde. The farmland consisted of north and south areas, which hereafter will be called as the Northern field and the Southern field. The soil moisture data were collected from June 2017 to July 2018. Different agricultural crops, e.g., wheat (planted in November 2017 harvested in July 2018), and corn (planted in August, until November 2018), are rotationally planted and at the Northern farm field. 13 out of 24 stations are located in the northern field, and the rest is located in the southern field. Stations 38 and 41 are located at the border zone between the two subsections, figure 2(a). The two stations are very close to station ITCSM10 of the Twente network, as presented in figure 2(b) & 2(c).

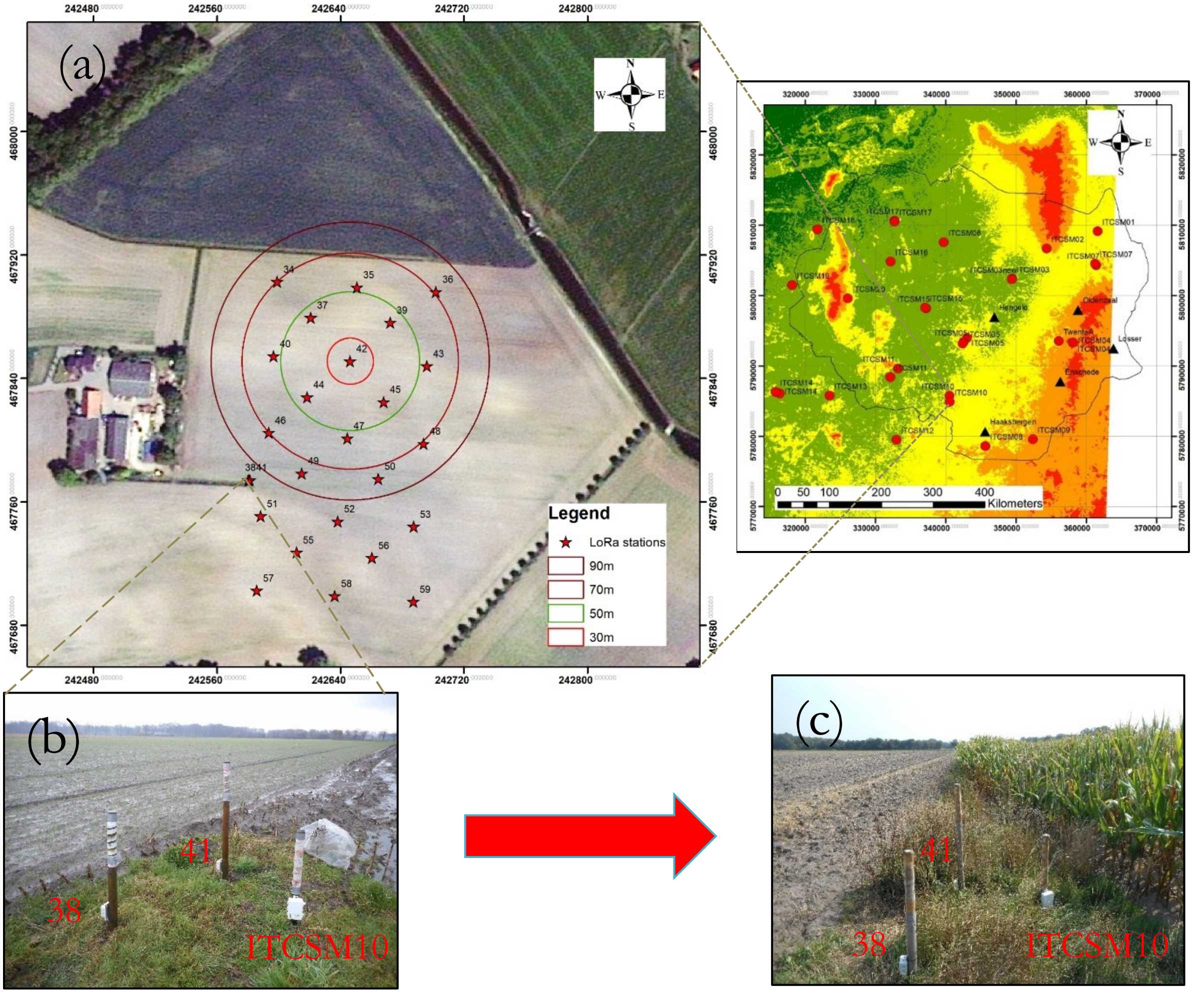

Figure 3 (a) Soil moisture measuring network known as LoRa network during the winter of 2017, (b) Installation of two extra LoRa units close to the soil moisture station at ITCSM10 on 2018/02/02. (c) The situation of fields and the soil moisture stations at ITCSM10 on 2018/07/11.

2.4. Soil moisture monitoring networks instrumentation

The Decagon 5TM sensors Decagon (2016), have been installed to measure Volumetric water content and Soil temperature every 15 minutes. The accuracy of Volumetric water content and Soil temperature is ± 0.03 m3/m3 (± 3% VWC) and ± 1°C, respectively. According to Nyamu (2019), the estimated calibration coefficients for the Volumetric water content sensor are 1.758 and 0.020 for a and b, respectively. The sensors are usually placed vertically to minimize ponding problems. The 5TM sensors use an oscillator at 70MHz to measure soil capacitance, which is convertible to the dielectric permittivity of the soil. The dielectric permittivity of the soil is then used to calculate volumetric soil moisture (Dobson et al., 1985).

2.5. Ancillary data

2.5.1. Temperature data

Figure 3 shows the minimum value of the temperature of in-situ measurements for the Twente region from 1st December 2017 to 7th July 2018 on a daily basis (https://www.knmi.nl/nederland-nu/klimatologie). The obtained air temperature values reached below the freezing point (at 1 degree Celsius) in February 2018.

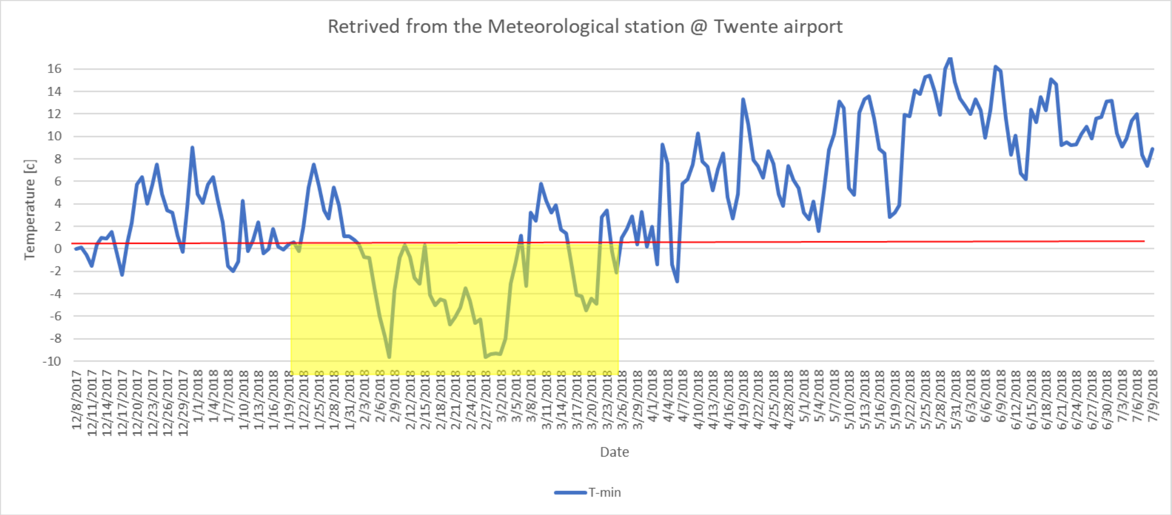

Figure 4 The air temperature data at 10 cm above the surface collected from the weather station in Twente airport

2.5.2. Land cover data

The landcover is categorized into 15 different landcover classes demonstrating high land surface heterogeneity. More than 80 percent of the Netherlands is utilized for agriculture, recreation, woodlands, and nature, as seen through the different shades of green color in figure 5. Agriculture is the primary land-use activity for the Dutch, mainly growing corn, potatoes, wheat, etc. the red color shows the urban areas. A large concentration of urban areas is located in the western part of the Netherlands. In contrast, significantly less urban areas are placed in the Eastern part of the Netherlands.

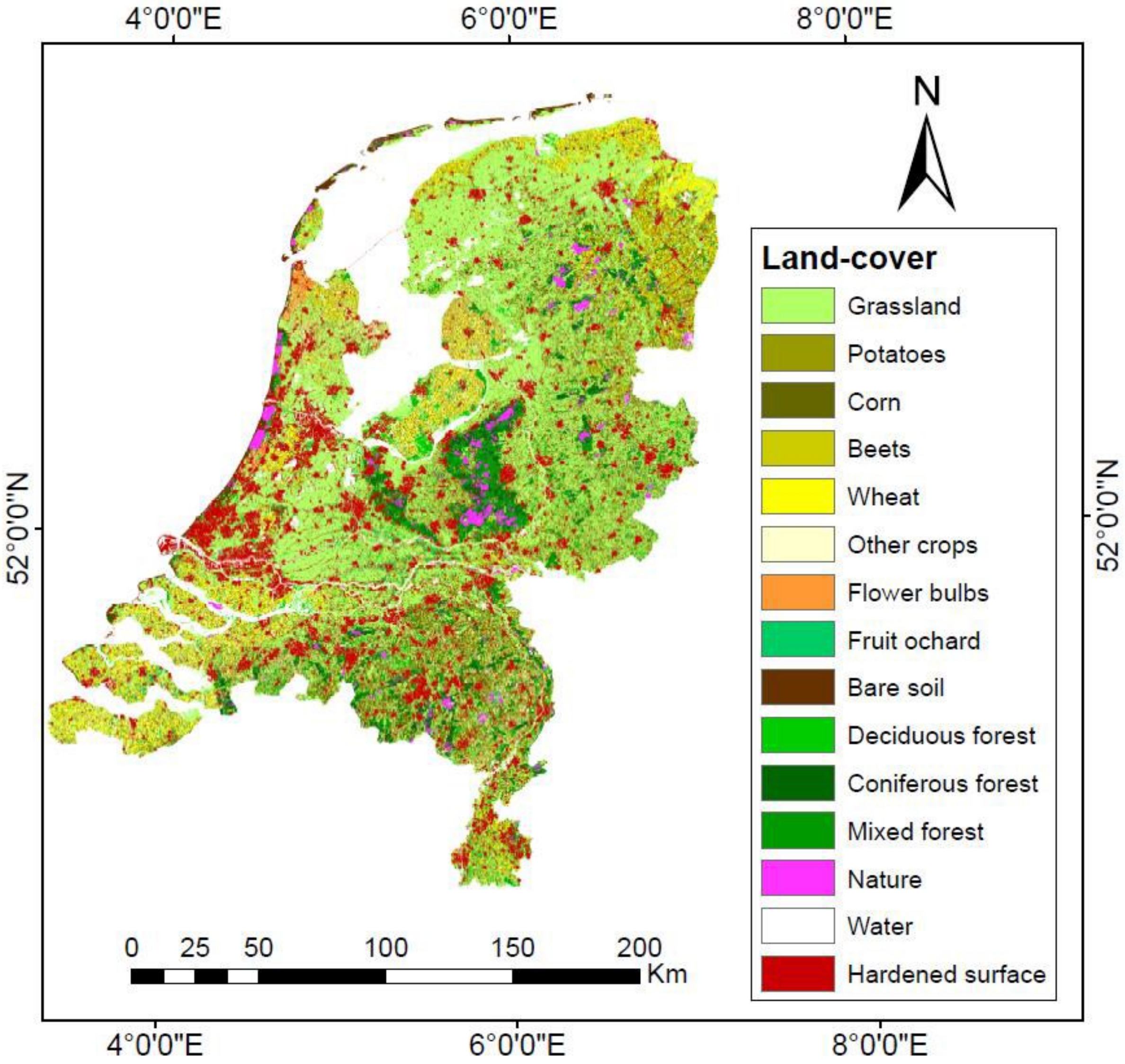

Figure 5 Landcover map for the Netherlands (https://www.clo.nl/node/20807)

3. REMOTE SENSING DATA

The Copernicus Programme is sponsored by the European Union and supported by the European Space Agency (ESA). The Copernicus program aims are to provide a world-wide, nonstop, independent, high quality, a wide range of Earth observation capacity.

3.1. Sentinel-1 A/B

Sentinel-1 A/B is part of the Copernicus mission. It collects a wide range of C-band SAR backscattering observations at different polarizations and resolutions. The collected data from Sentinel-1 contains Level-1 Ground Range Detected (GRD) which is processed to deliver backscatter observations ($\sigma°$) converted to decibels (dB) as $10*\log10\sigma°$. Sentinel-1 VV observations were collected via the Google Earth Engine platform (Gorelick et al., 2017). A pixel in the grid image of Sentinel-1 Interferometric Wide Swath (IW) is resampled to 10 by 10 m area to represent a 100 m^2 area. The characteristics of Sentinel-1 (IW) are described in table 1.

Table 1 Characteristics of Sentinel-1 Interferometric Wide Swath Instrument

Platform	Sentinel-1 A/B
Acquisition Date	2015 - Current
Instrument Mode	'IW' (Interferometric Wide Swath)
Altitude	693 km
Orbit	Ascending/Descending
Band	C-band
Frequency	5.405 GHz
Wavelength	1530–1565 cm
Polarization	VV
Incident Angle	34-45˚degree
Inclination Angel	98.18 degree
Period	98.6 min
Grid resolution	10 m
ground coverage	~50×70 km

3.1.1. Sentinel-1 filtering and Pre-processing

Meanwhile, collected data need several pre-processing steps to obtain calibrated, orthorectified imagery. This section designates the data collection and pre-processing steps of Sentinel-1. Google Earth Engine follows the same pre-processing steps as implemented by the Sentinel-1 Toolbox to apply Thermal noise, Radiometric, and Terrain corrections in each pixel (Veci, 2015).

3.2. Sentinel-2 A/B

Relatively new earth observation satellite Sentinel-2 A/B is part of the European Copernicus Program. The Sentinel-2 mission aims to provide pieces of information for various applications such as spatial planning, agriculture, vegetation monitoring, and drought assessment. One of the advantages of Sentinel-2 is the improved spatial and spectral resolution, which subsequently improves our ability to estimate vegetation indices. The improved vegetation indices from Sentinel-2 with 10 meters spatial resolution should dedicate an improvement to monitor vegetation water content. Twelve bands of The Sentinel-2 contain 16 bits radiometric resolution. Apart from that, the Sentinel-2 mission has a temporal resolution of 2 times a week over the Netherlands on average, which gives an excellent insight into the time-series variation of vegetation. The characteristics of the Sentinel-2 Multi-Spectral Instrument (MSI) are described in table 2.

Table 2 Characteristics of Sentinel-2 for Multi-Spectral Instrument

Platform	Sentinel-2 A/B
Acquisition Date	2016 - Current
Instrument Mode	Multi-Spectral Instrument (MSI)
Altitude	786 km
Revisit time	2-3 days at mid-latitudes
Spectral Bands	Visible and Near-Infra-Red (VNIR) bands
spatial resolution	10 m
Wavelength	0.66 – 0.78 (μm)
Field Of View (FOV)	290 km
Incident Angle	34-45°degree
Inclination Angle	98.62 degree

3.2.1. Sentinel-2 Cloud Filtering

The Sentinel-2, Level-2 (S2L2) data products are explored and extracted from the Google Earth Engine (GEE). The S2L2 removes atmospheric errors and provides Bottom of Atmosphere (BoA) reflectance. Band 3 (559.8 nm) and Band 10 (1373.5 nm) designing a decision tree for detecting and removing the clouds from S2L2 observations Hollstein, Segl, Guanter, Brell, & Enesco, (2016), as shown in figure 6:

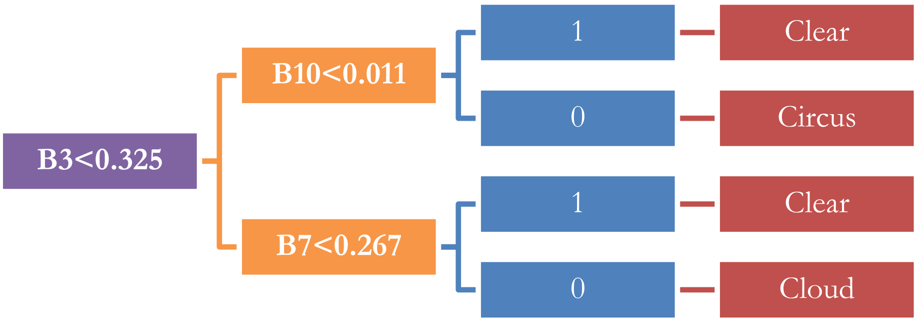

Figure 6 Decision tree of cloud filtering

3.3. Data access via Google Earth Engine

Google Earth Engine associate with a multi-million-byte repository of satellite images and geospatial datasets. The capabilities and planetary-scale analysis of Google Earth Engine ease data mining for scientists, researchers, and developers. To access the data via GEE, a user must use a Gmail account and sign up at https://earthengine.google.com/.

Note that Google Earth Engine charges users for commercial purposes. However, the service is free for students and researchers. The Sentinel-1 and Sentinel-2 datasets are called via:

```
ee.ImageCollection('COPERNICUS/S1_GRD')
ee.ImageCollection('COPERNICUS/S2')
```

The collected data should be filtered out via the filtering functions. All the processing steps to collect, filter, and extract the data via GEE will be described in section 6.

4. METHODS

4.1. Normalized Differential Vegetation Index (NDVI)

NDVI was the first time introduced by (Rouse et al., 1973). It is a numerical value that is calculated based on the intensity of reflected light in near-infrared range minuses the red range divided by the sum of these intensities, as shown in Eq. 1.

$$NDVI = (NIR - Red) / (NIR + Red) \qquad (1)$$

NDVI is implemented to evaluate the bio-physical property (i.e., density) of vegetation from the observed target. The values are ranging from -1 to 1. Values below -0.1 correspond to water bodies. Values close to zero between (-0.1 to 0.1) correspond to bare soil (i.e., sand, rock, or snow).values ranging between 0.1 and 0.6 correspond to light vegetation land cover (i.e., grassland, and farmland). Lastly, values higher than 0.6 correspond to highly dense vegetation (i.e., forest, tropical rainforests) (Kumar, Rao, & Sharma, 2013).

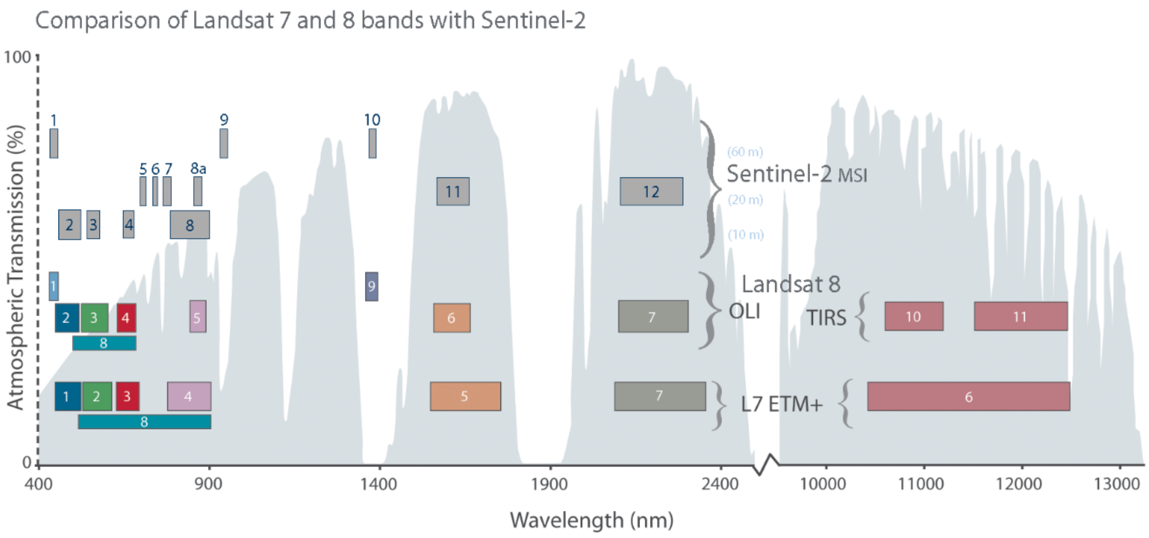

Figure 7 present the spectral bands of sentinel-2---cite

The red band (band 4) and near-infrared band (band 8) have a spatial resolution of 10 meters. However, the narrower bands in the "red-edge" (i.e., bands 5, 6, 7) with the 20-meter spatial resolution are explicitly related to monitoring vegetation and agricultural studies. The broad spectral range in band 8 of Sentinel-2 (0.76-0.90 µm) is more subjected to the atmospheric attenuation due to water vapor particles in the atmosphere. In contrast, band 7 (0.76-0.79 µm) is located at the atmospheric window avoiding the atmospheric attenuation due to water vapor (0.80-0.82 µm), as shown in figure 7. Moreover, according to Feng et al., (2020), the estimated vegetation indices using wavelengths located in the red edge can estimate the NDVI more accurately than standard NDVI.

4.2. Integrating the Water Cloud model with IEM

The amount of vegetation grows consistently and effectively, an obstacle to simulating backscattering values accurately. The Water Cloud model (WCM) is a radiative transfer model that calculates the attenuation and scattering by vegetation. WCM was integrated with IEM simulation to account for the vegetation effects, as shown in Eq.s [2-5]:

$$\sigma_{soil}^{0}[\frac{m2}{m2}] = 10^{\left(\frac{\sigma_{Sentinel1}\,[dB]}{10}\right)} \tag{2}$$

$$\sigma_{total}^{0}(\theta) = \sigma_{v}^{0}(\theta) + \gamma^{2}\sigma_{soil}^{0}(\theta) \tag{3}$$

$$\sigma_{v}^{0}(\theta) = (1-\gamma^{2})A.V_{1}\cos\theta \tag{4}$$

$$\gamma^{2} = exp\left[\frac{-2B.V_{2}}{\cos\theta}\right] \tag{5}$$

Where the backscattering observation in bare soil (σ_{soil}) is converted to intensity units (m2/m2) to remove the vegetation effect, as expressed in Eq. (2). The total backscattering observation (σ_{total}^{0}) is calculated by integrating the IEM with the WCM, as expressed in Eq. (3). WCM requires calibrated values of crop factors (*A, B*) to eliminate vegetation effect including the vegetation attenuation process (γ^{2}), expressed in Eq. (4), and the scattering process between the vegetation and the soil (σ_{v}^{0}), expressed in Eq. (5). The crop water content (*V_1, V_2*) can be estimated by spectral Vegetation Indices (VIs) (F. Zhang & Zhou, 2019). This study uses the NDVI values as an indicator of crop water content. Therefore, the obtained NDVI values from S2L2 are used as the crop water content (*V_1, V_2*) to calibrate the vegetation crop factors (*A, B*) for winter wheat and corn. In the integrated model, the calculated total backscatter would be equivalent to the surface backscattering model if the crop water content is zero.

4.3. Retrieving soil moisture via inverse WCM

As was discussed in the previous section, simulating backscattering observations of Sentinel-1 C-band requires comprehensive knowledge about the ground surface and the crop water content. However, to retrieve soil moisture the calculated total backscattering coefficient (σ_{total}^{0}) should be replaced with obtained backscattering observations from Sentinel-1. As a result, the backscattering observations from Sentinel-1 become the input, and the retrieved soil moisture will be the output to the inversed integrated model. Using Eq. (2)The collected backscattering observations from Sentinel-1 should be converted to intensity units (m2/m2) to remove the vegetation effect. Then the result should be converted to Decibel.

4.4. Root mean square error

The Root Mean Square Error (RMSE) plays two essential roles in this study. First, it was used as a cost function, for optimizing roughness parameters and crop factors. Second, it was used for assessing the accuracy of calculated simulation compared to the actual observations and ground measurements. The general term of RMSE, as shown in Eq. [6]:

$$RMSE\ [unit] = \frac{\sum\sqrt{(measurment[unit] - simulation[unit])^{2}}}{N} \tag{6}$$

Where N is the number of observations at each iteration.

4.5. Pearson correlation coefficient (r)

Pearson's correlation coefficient is a statistics test which can calculate the statistical relationship between two-time series variables. It tries to make the best fit via the observations and simulation results. The Pearson correlation coefficient (r) shows how these two datasets are correlating in time, as shown in Eq. [7].
The value of “r” ranges from +1 to -1, where 0 means no correlation. As r moves toward +1, the fit via the observations and simulation results become stronger.

$$r = \frac{n(\sum xy) - (\sum x)(\sum y)}{\sqrt{[n\sum x^2 - (\sum x)^2][n\sum y^2 - (\sum y)^2]}} \tag{7}$$

5. RESULTS AND DISCUSSION

5.1. Spatial and temporal matching

5.1.1. Soil Moisture Analysis

The retrieved soil moisture is not equivalent to the soil moisture values obtained by the LoRa network because soil moisture is highly variable. The spatial resolution of Sentinel-1 is equivalent to 12.5 meters while the distance between LoRa stations between the stations is a=35 m and the diagonal distance between stations is $a\sqrt{2}{\sim}50m$. As a result, taking the daily basis average of soil moisture and aggregated sentinel-1 backscattering values at 50 m should deliver a better match between the two variables. The LoRa station "42" was selected as the center of the northern farm field. We took the mean of SMC values based on four different area-subsets around station 42. The mean of 24 hours value of SM was calculated at the identified subsets. The list of stations involved in calculating the average values is shown in table 3.

Table 3 List of stations involved to obtain the average values

Spatial Extend	Stations for averaged subsets
10m from '42'	42
30m from '42'	39,40,42,43
50m from '42'	37,39,42,44,45
70m from '42'	35,37,39,40,42,43,44,45,47
90m from '42'	34,35,36,37,39,40,42,43,44,45,46,47,48

Moreover, the statistical summary of the calculated mean of soil moisture in five different subsets is presented at table 3. According to table 4, as we changed the spatial subset of soil moisture from 10-m to 90-m and increases the area, the mean of soil moisture increases from 0.22 to 0.28 m^3/m^3.

Table 4 Statistical summary of averaged soil moisture values at five different subsets

Soil moisture	Mean [m3/m3]	Std [m3/m3]	Max [m3/m3]	Min [m3/m3]
ITCSM_10	0.29	0.12	0.50	0.10
10m from '42'	0.22	0.13	0.49	0.04
30m from '42'	0.25	0.14	0.57	0.05
50m from '42'	0.27	0.15	0.55	0.05
70m from '42'	0.27	0.16	0.58	0.05
90m from '42'	0.28	0.16	0.58	0.06

In addition to the LoRa network, one of the Twente network monitoring stations, ITCSM10 is located at the corner of the northern farm field. The obtained soil moisture values were compared with the collected data at ITCSM10 station. Table 4 compares the daily average of soil moisture values from the LoRa network with ITCSM10 station. It was observed that the daily average of soil moisture of the whole farmland has become extremely close (0.28 m3/m3) to the daily average of soil moisture value at ITCSM10 (0.29 m3/m3).

Besides, we performed a comparison between the averaged values of LoRa network with the soil moisture data from ITCSM10 using a daily basis correlation function with a time window of 30 days and then calculate correlation values between the backscattering values of sentinel-1 and the ground measurements of soil moisture in the same area.

Table 5 statistical summary of the correlation between the soil moisture values of ITCSM_10 and LoRa Stations at five different subsets

	ITCSM_LORA10	ITCSM_LORA30	ITCSM_LORA50	ITCSM_LORA70	ITCSM_LORA90
Mean	0.63	0.67	0.67	0.67	0.68
Std	0.16	0.14	0.14	0.14	0.14
Max	0.96	0.95	0.96	0.95	0.96
Min	0.11	0.24	0.23	0.17	0.20

According to table 5, we observe that the soil moisture variation and the correlation rate between ITCSM10 and the spatial average of the LoRa network in a different area of subsets. ITCSM10 generates a Pearson correlation coefficient of 0.68 with a daily average of soil moisture data collected at a 90-m subset. Such a strong correlation value indicates that soil moisture data collected from station ITCSM10 can also be a good representative of the whole extend of the North field. Due to a drop in air temperature belong to the freezing point, The correlation values between the two soil moisture datasets drop dramatically for 28 days (between 23 of February until 21 March 2018). The soil moisture at different points started to freeze, while this might not be the case for other stations. As a result, higher spatial variability in soil moisture will be observed, and the correlation between ITCSM10 and the daily average of soil moisture from LoRa network drop dramatically during this period as is shown in Figure 8.

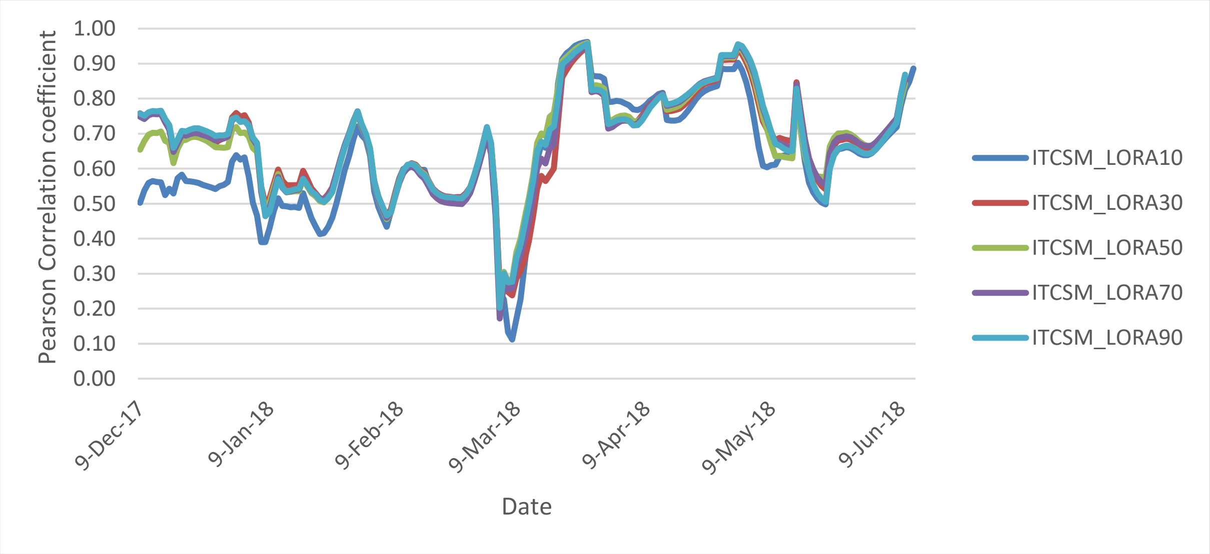

Figure 8 correlation between soil moisture values at ITCSM_10 and the mean of Lora based soil moisture observations at five different subsets

5.1.2. Backscatter Analysis

In the same manner, the backscatter observations were calculated by taking the average of Sentinel-1 pixels values at five different subsets (e.g., 1-by-1, 3-by-3, 5-by-5, 7-by-7, and 9-by-9 pixels) centered on LoRa station 42. The subsets are covering areas ranging from 10 to 90 m away from the center of the north field. Table 1 presents the statistical summary of backscatter values at five different subsets. According to table 6, the standard deviation of observation at larger subsets has become relatively smaller, which indicates lower spatial variability.

Table 6, Statistical summary of backscatter values at five different subsets

Sentinel-1	Mean	std	Max	Min
10m from '42'	-11.37	3.08	-3.64	-18.10
30m from '42'	-11.08	3.00	-4.11	-17.60
50m from '42'	-11.16	2.66	-4.92	-16.53
70m from '42'	-11.25	2.71	-5.76	-16.78
90m from '42'	-11.72	2.37	-5.25	-17.49

According to (Benninga, van der Velde, & Su, 2019), weather conditions negatively affect the sentinel-1 backscattering observations, and specific masking rules are required to follow. Therefore, to better analyze the behavior of sentinel-1 backscattering observations, it is necessary to consider the weather conditions, i.e., temperature and precipitation. The obtained air temperature data, shown in figure 4, shows that there is a gradual drop in air temperature below 1 degree of Celsius between 23rd February and 23th March 2018. Such a freezing condition is likely to disturb the backscattering observation at this period. No significant rainfall was observed for this period.

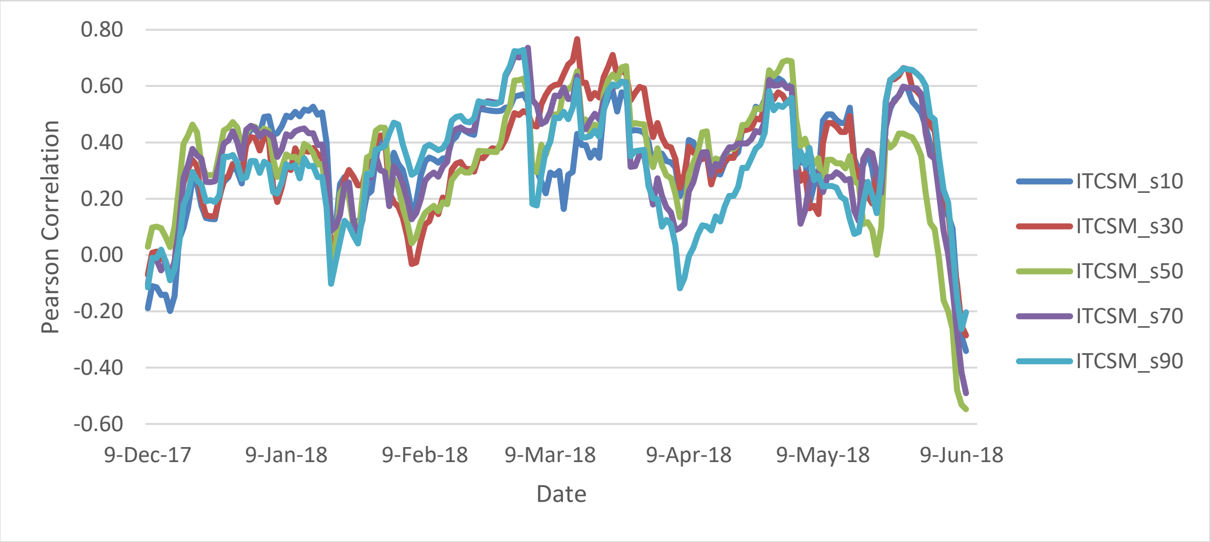

Figure 9 Pearson correlation between soil moisture values at ITCSM_10 and backscatter values of Sentinel-1 at five different subsets

Moreover, knowing that the vegetation growth rate is much slower than the variations of the weather. It is assumed that the variation of vegetation is constant for 30 days. Consequently, the Pearson correlation coefficient between the soil moisture values at ITCSM10 and the collected backscattering values from sentinel-1 was computed. According to figure 9, there is a moderate correlation coefficient (between -0.22

and 0.60 percent) between the soil moisture collected from ITCSM10, and sentinel-1 backscatter values is observed.

The Pearson correlation coefficient is a single number that represents the level of association between two sets of measurements. Correlations are usually worked out based on samples from populations. However, their interpretation becomes difficult as the correlation value can be affected by the size of the sample. As a result, the obtained correlations with small samples are quite unreliable. For example, we take two samples of measurements from these variables and perform a correlation test on them daily. Our correlation test will produce a value of r that is 0, or close to 0. If this procedure is repeated many times, the sample correlation coefficient can be much larger or smaller than the true population because samples vary randomly from time to time.

In other words, on occasion, there will be large values of r that have really occurred by chance but might mislead us into thinking that there was a strong correlation in the parent population. The smaller the sample size, the higher the likelihood of obtaining a spuriously-large correlation coefficient. As a result, to obtain reliable correlation values, compare the forward and backward correlations.

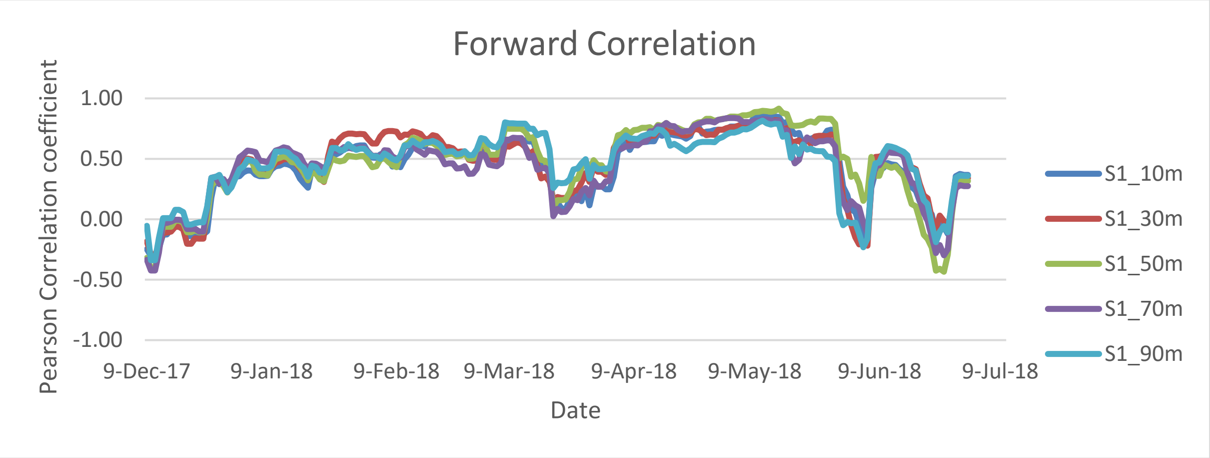

Figure 10 forward correlation between soil moisture values of LoRa Stations and backscatter values of Sentinel-1 at five different subsets

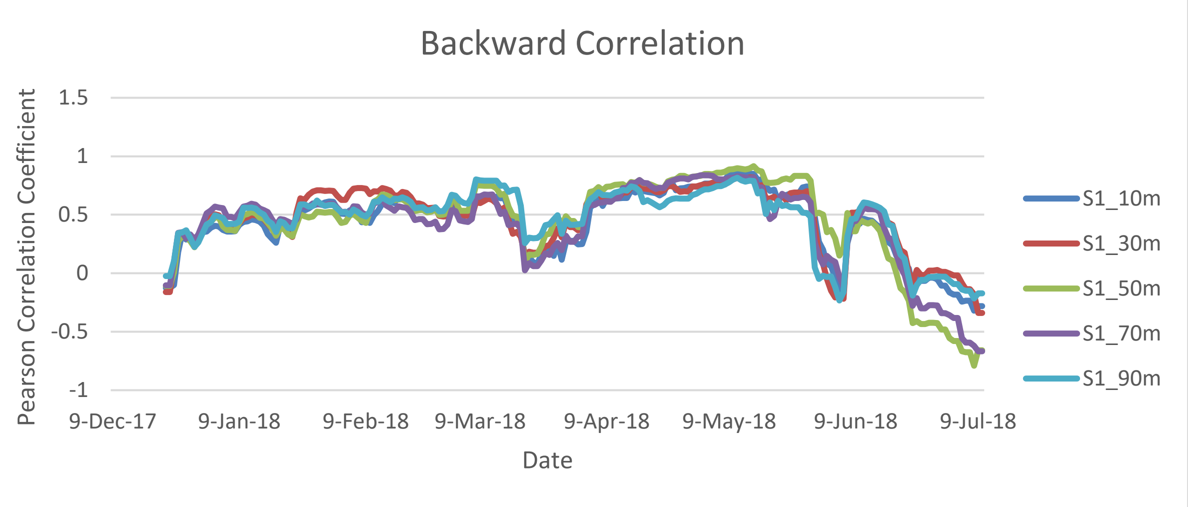

Figure 11 backward correlation between soil moisture values of LoRa Stations and backscatter values of Sentinel-1 at five different subsets

In forward correlation, we start with 15 observations beginning from 9 December 2017 and add one more observation for every time step until we reach to 24 December, which is 15 days after the first observation to make a kernel of 30 days, figure 10. Then we move the kernel forward until it reaches the last value of observations. In backward correlation, we do the same procedure, but we start from the last observation on 7 July 2018 and move the kernel window backward to the first observation, figure 11.

The calculated correlation coefficients between the spatial **mean** of the LoRa network and the spatial **mean** of sentinel-1 backscatter observations for different subsets are presented in table 6. According to table 6, it is noticed that there is a sharp drop between 23 Feb and 21 March 2018. The land cover at this period is continuously bare soil, and the only variable that can affect this decorrelation is soil temperature below the freezing point, which has been observed for the same period.

Table 7 statistical summary of the correlation between the soil moisture values of LoRa Stations and backscatter values of Sentinel-1 at five different subsets

	Forward Correlation					Backward Correlation				
	10m	**30m**	**50m**	**70m**	**90m**	**10m**	**30m**	**50m**	**70m**	**90m**
Mean	0.48	0.52	0.53	0.49	0.51	0.49	0.53	0.53	0.50	0.52
Std	0.23	0.23	0.27	0.24	0.22	0.23	0.22	0.26	0.23	0.21
Max	0.85	0.82	0.92	0.84	0.82	0.85	0.82	0.92	0.84	0.82
Min	-0.18	-0.22	-0.43	-0.30	-0.23	-0.18	-0.22	-0.43	-0.30	-0.23

5.1.3. Temporal matching

Sentinel-1 collects instantaneous observations (11 ascending, ten descending), which provide 21 observations on average every month. The ascending observations are captured roughly at 5:30 p.m. The Descending observations are captured at 5:30 a.m. We took the instantaneous spatial mean of soil moisture values and the daily average to compare correlation values between them.

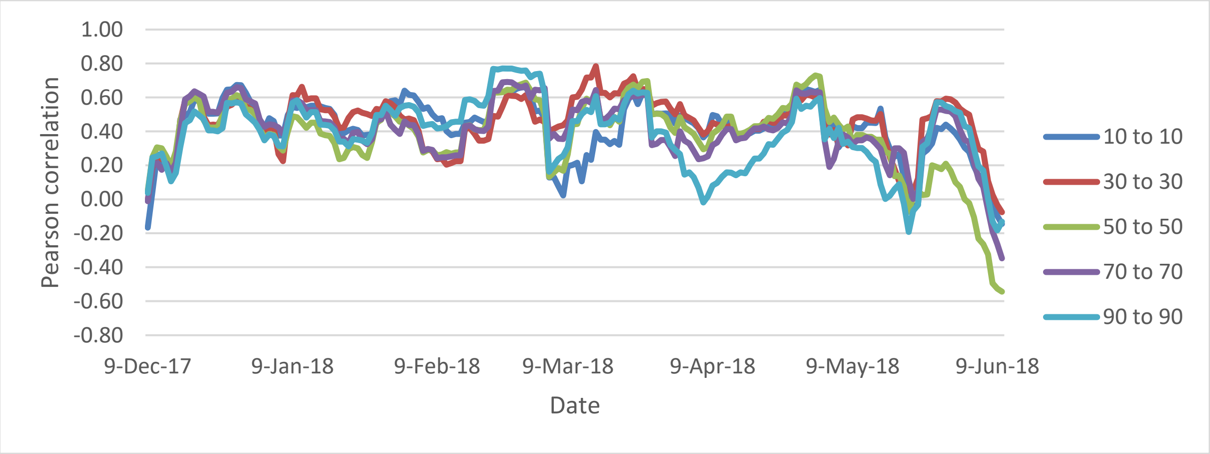

Figure 12 Pearson Correlation values between S1 and instant values of SMC from LoRa Network

Due to soil composition, rain takes a significant time to arrive at the soil moisture sensor (Nieber, 1982). Therefore, a delay between the soil moisture measured by the sensor and the surface soil moisture affecting Sentinel-1 is likely to occur. Comparing the instantaneous values of soil moisture measurements with a daily average of soil moisture shows that the daily average obtains better correlation than the instantaneous values, as shown in table 8. Moreover, the daily average of 50-m subset obtained a correlation value of 0.56, which is the highest correlation value compared to other subsets. As a result, the daily average of a 50-m subset was selected to be used for calibration of roughness parameters for the wheat field.

Table 8 compares correlation values between the spatial mean of soil moisture values and the daily average

	The daily average of soil moisture					The instantaneous spatial mean of soil moisture				
Subset	**10 to 10**	**30 to 30**	**50 to 50**	**70 to 70**	**90 to 90**	**10 to 10**	**30 to 30**	**50 to 50**	**70 to 70**	**90 to 90**
Mean	0.44	0.44	0.56	0.49	0.50	0.44	0.41	0.45	0.44	0.41
Std	0.35	0.36	0.28	0.29	0.28	0.23	0.28	0.26	0.25	0.30
Max	0.91	0.88	0.90	0.86	0.94	0.85	0.83	0.85	0.86	0.93
Min	-0.54	-0.56	-0.46	-0.40	-0.41	-0.34	-0.42	-0.37	-0.21	-0.40

5.2. Calibration and validation of roughness parameters for the wheat field

The calibration of the IEM to specific roughness parameters is required to obtain accurate backscattering coefficients. A lookup table (LUT) method was used to estimate backscattering coefficients for several roughness parameters, iteratively. The forward IEM was performed to simulate the backscattering coefficient for bare soil surface using the observed soil moisture via the given surface roughness and Sentinel-1 configuration parameters. The observed soil moisture values were converted to dielectric constant values via Dobson et al. (1985).

The LUT generates unrepeatable pairs of Roughness parameters RMS height (s) and correlation length (l) by keeping l as constant and counting on the s value. The number of paired values depends on the given range and the intervals of s, l. The valid range of s for the IEM at C-band should be $ks < 3.0$, with k being the wavenumber $2\pi/\lambda$ of radar signal $k = 1.11$ cm^{-1} for C-band, and λ is the wavelength. This means that s for Sentinel-1 c-band should be less than 3 cm. The given$s$ ranged from 0.1 to 3 cm with $\Delta s = 0.1$ cm for C-band. For correlation length, the surface profile was described using a linear function. An upper bound of 20 cm and a lower bound of 3 cm were applied during the iteration process with $\Delta l = 0.1$ cm. The RMS height and correlation length were set to s=0.01 and l=3 cm as an initial value. All different pairs of roughness parameters (s,l) were tested as the input to estimate backscattering values for over 56400 times iteration. Multiplying this with the number of observations and will give an enormous number of iterations. For example, if we perform the process only for observations, over 200,000 iterations should have been performed, as shown in table 9.

Table 9 Show an example of the LUT for inserting the frequency, incident angle, the roughness parameters, and dielectric constant in IEM

Iteration	Frequency	Theta	l	s	Dielectric constant	
	[Ghz]	[Degree]	[cm]	[cm]	Real	Imaginary
1	5.405	37.67	3	0.01	10.37192	2.000973
2	5.405	44.62	3	0.01	9.524886	1.766825
3	5.405	44.66	3	0.01	8.972604	1.615974
4	5.405	37.68	3	0.01	6.667947	1.006719
5	5.405	37.67	3	0.02	10.37192	2.000973
6	5.405	44.62	3	0.02	9.524886	1.766825
7	5.405	44.66	3	0.02	8.972604	1.615974
8	5.405	37.68	3	0.02	6.667947	1.006719
9	5.405	37.67	3	0.03	10.37192	2.000973
10	5.405	44.62	3	0.03	9.524886	1.766825
11	5.405	44.66	3	0.03	8.972604	1.615974

12	5.405	37.68	3	0.03	6.667947	1.006719
.	.	.	.	.	.	.
.	.	.	.	.	.	.
.	.	.	.	.	.	.
205193	5.405	37.67	20	2.99	10.37192	2.000973
205194	5.405	44.62	20	2.99	9.524886	1.766825
205195	5.405	44.66	20	2.99	8.972604	1.615974
205196	5.405	37.68	20	2.99	6.667947	1.006719
205197	5.405	37.67	20	3	10.37192	2.000973
205198	5.405	44.62	20	3	9.524886	1.766825
205199	5.405	44.66	20	3	8.972604	1.615974
205200	5.405	37.68	20	3	6.667947	1.006719

It is necessary to divide the obtained data into calibration and validation sets as training and testing independently to check the accuracy of optimization results. It is expected that the more extended data dedicated to calibration, the more accurate optimization results will be achieved. Therefore, initially, out of four months of bare soil 2 months from 1st December 2017 to 31th of January 2018 were dedicated to the calibration process, and two months, from 1st of February to 31th of March, was dedicated to the validation period, as shown in table 10.

Table 10 present the dedicated validation and calibration periods for checking the optimization process

Paths	December 2017	January 2018	February 2018	March 2018
Ascending	**Calibration**		**Validation**	
Descending	**Calibration**		**Validation**	

5.2.1. The calibration process of roughness parameters for the wheat field

Ascending observations looked a bit noisy during February 2018 due to the freezing soil temperature. Therefore, the calibration process to obtain roughness parameters required more observations for training and, therefore, was extended to three months instead of two months observations that was dedicated initially. For each pair of roughness parameters, the IEM iterate to calculate the backscattering coefficient. Each iteration updates a new pair of surface roughness parameters and goes to the next iteration until all the RMS height, and the correlation length values are complete.

Moreover, for each pair of given surface roughness parameters, the r and RMSE were computed using the observed and simulated backscattering coefficients. The minimum RMSE is used as the evaluation criteria to select the optimum surface roughness parameters, as shown in figures 12 & 13.

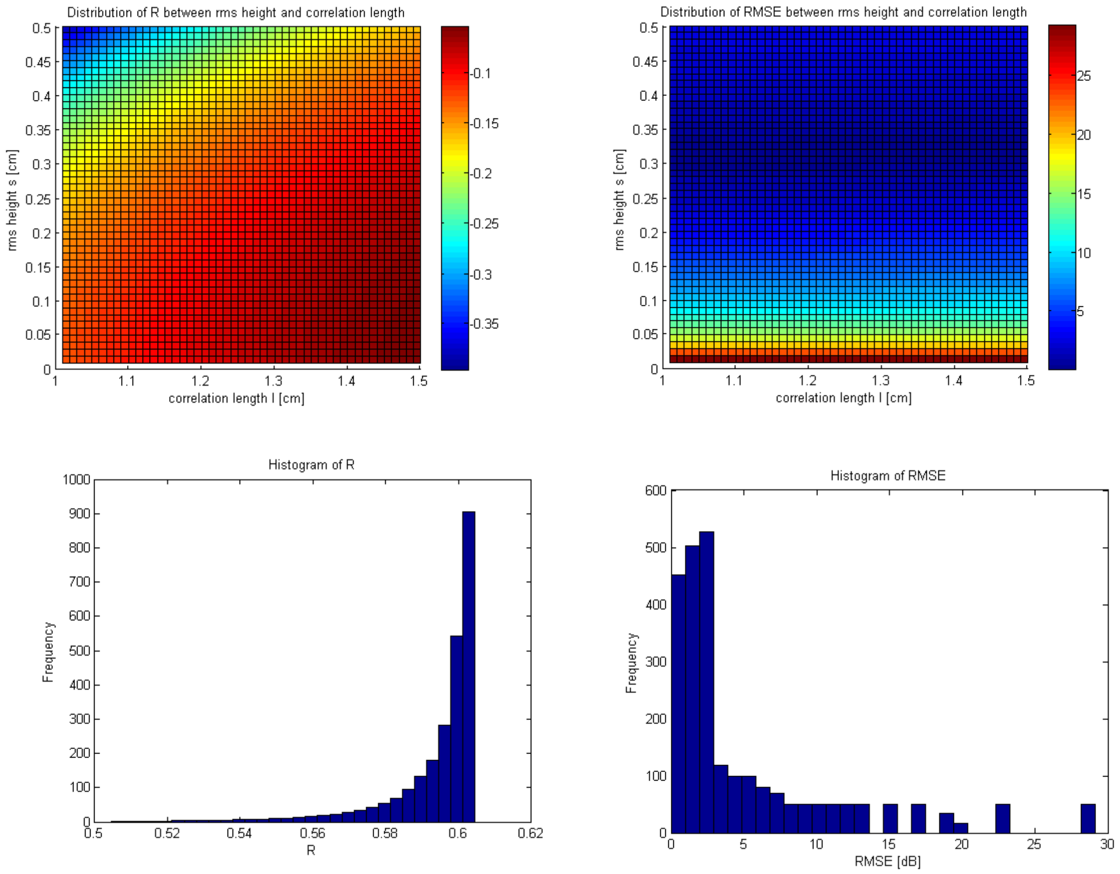

Figure 13 Distribution of R and RMSE between rms height and correlation length in ascending path

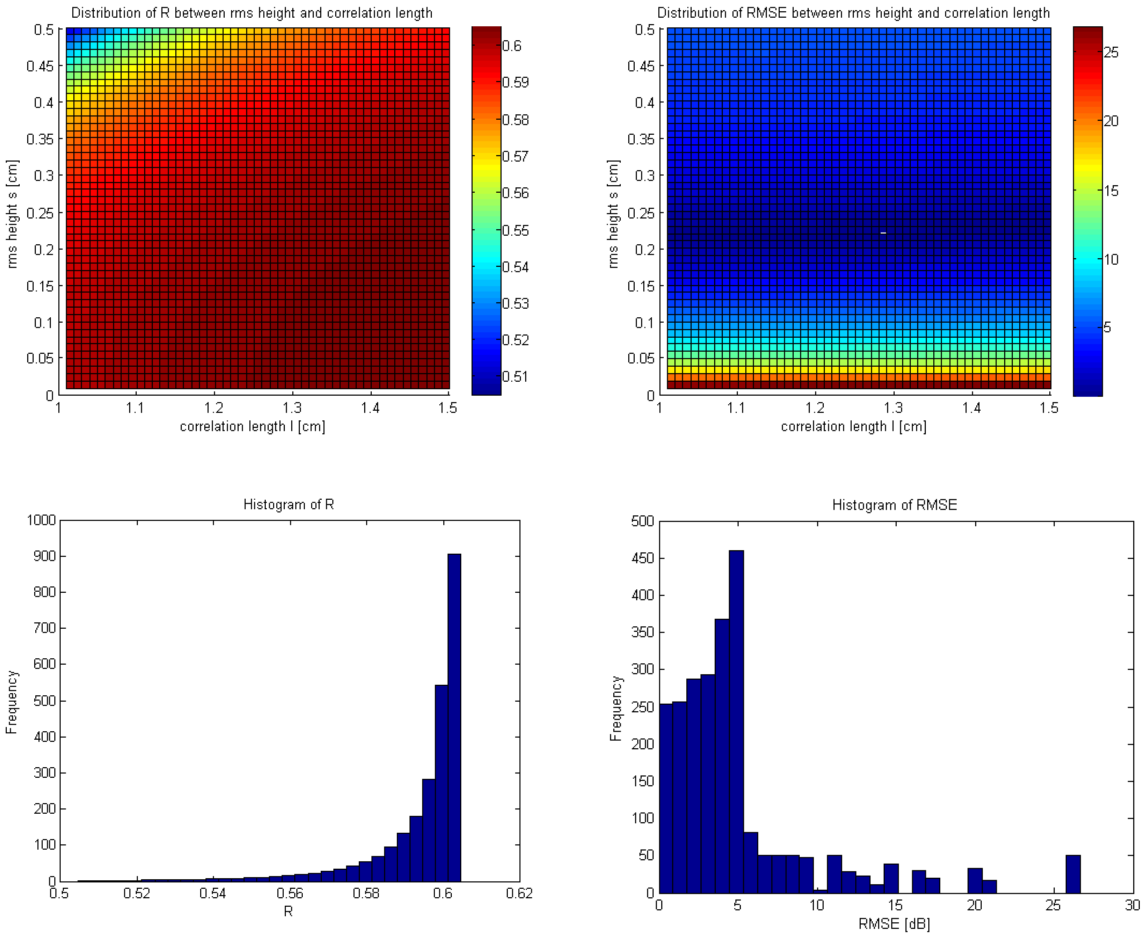

Figure 14 Distribution of R and RMSE between RMS height and correlation length in the descending path

The obtained results reflected that multiple combinations of roughness parameters (RMS height and correlation length) lead to the equal accuracy of simulated backscattering coefficients. This suggests that the obtained results have no unique solution for soil moisture retrieval. Therefore, under different combinations of RMS height and correlation length, it may produce a similar relationship between the soil moisture and backscattering coefficient (X. Zhang, Tang, Gao, & Zhao, 2018). This is the explanation of why there are multiple solutions for the optimum values. Nevertheless, the surface roughness parameters corresponding to the minimum RMSE values were selected as the optimum surface roughness parameters for ascending and descending orbits, as shown in table 11.

Table 11 shows obtained surface roughness parameters, RMSE, and the r based on simulated Daily basis backscattering coefficients for the wheat field.

Orbit path	*s*	*l*	RMSE [dB]	r
Ascending	0.39	3	1.48	0.62
Descending	0.26	3	1.43	0.52

The roughness parameters in ascending orbit were obtained 0.39 and 3 cm for RMS height (s) and length function (l), respectively. Meanwhile, the roughness parameters in descending orbit were obtained 0.26 and 3 cm for RMS height (s) and length function (l), respectively. The simulated and obtained backscatter observations for ascending and descending orbit paths are compared in Figures 14 and 15.

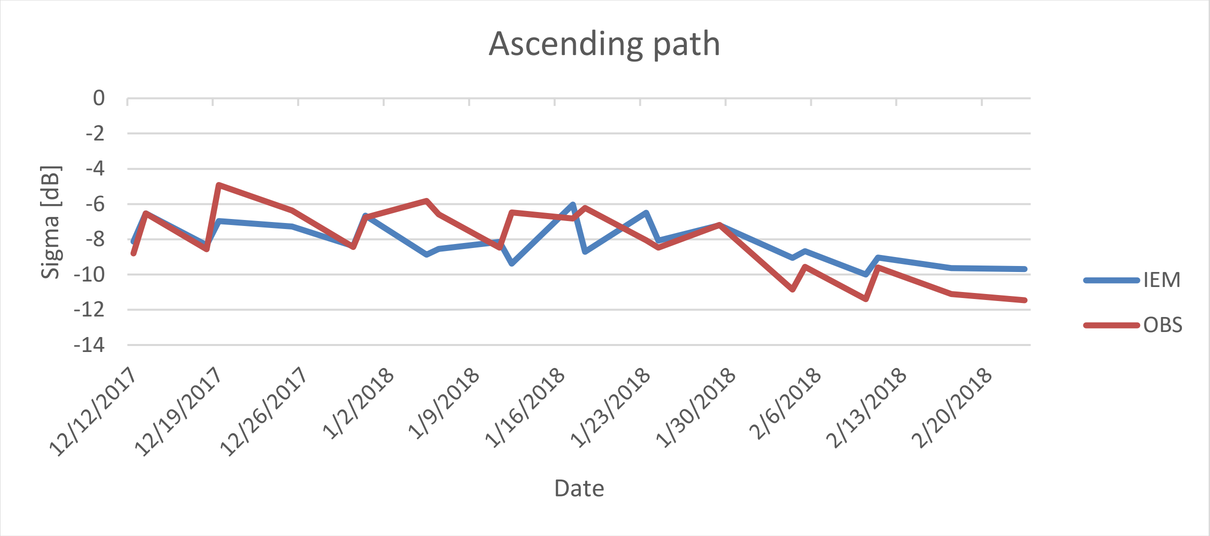

Figure 16. Compare simulated backscattering coefficients based and calibrated roughness parameters for ascending observations

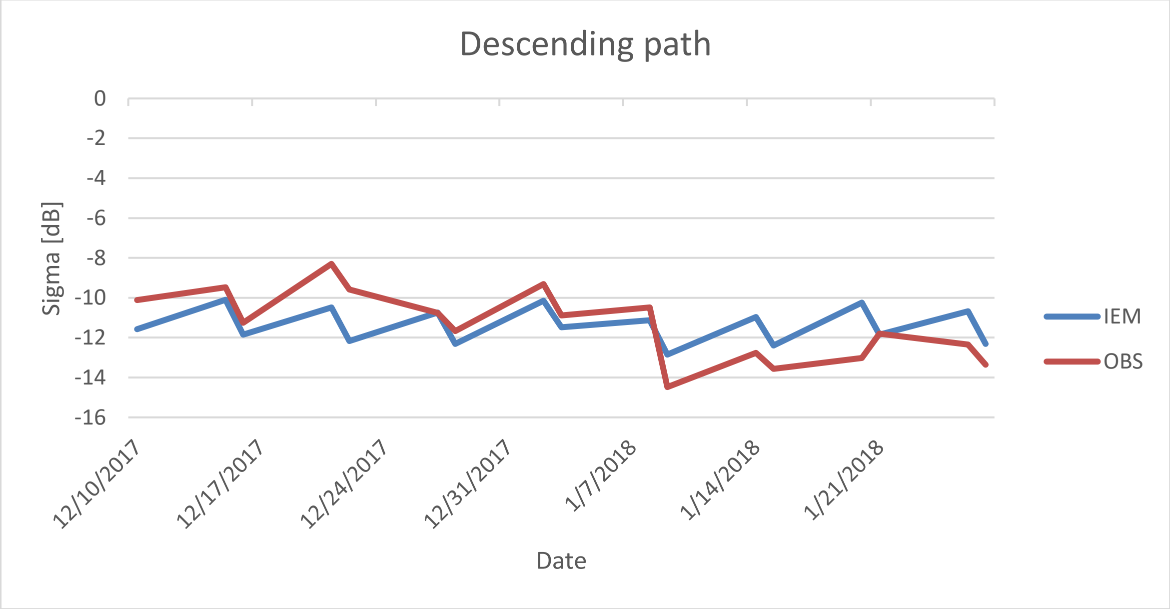

Figure 15. Simulated backscattering coefficients based and calibrated roughness parameters for descending observations

5.2.2. Validation of roughness parameters for wheat field:

The observed backscattering coefficients were selected from the 50-by-50 m subset, which is the area for which the highest correlation coefficient between the soil moisture and backscatter was found. We calibrated roughness coefficients to obtain the most accurate simulation results for ascending and descending observations separately.

When R is equal to its maximum and RMSE reached its minimum, the corresponding surface roughness parameters were chosen as the optimum surface roughness parameters. The selected RMS height and correlation length were tested via an independent set of observations from 1st to 31th of March 2018, for ascending and descending paths independently.

The backscattering coefficients for optimized roughness coefficients do fit in the acceptable range. The obtained results show a significant improvement in the accuracy of simulated backscattering coefficients (r=0.62, RMSE=1.4 dB) and (r=0.55, RMSE=1.4 dB) for ascending and descending paths, respectively, as it is shown in figure 16, and 17.

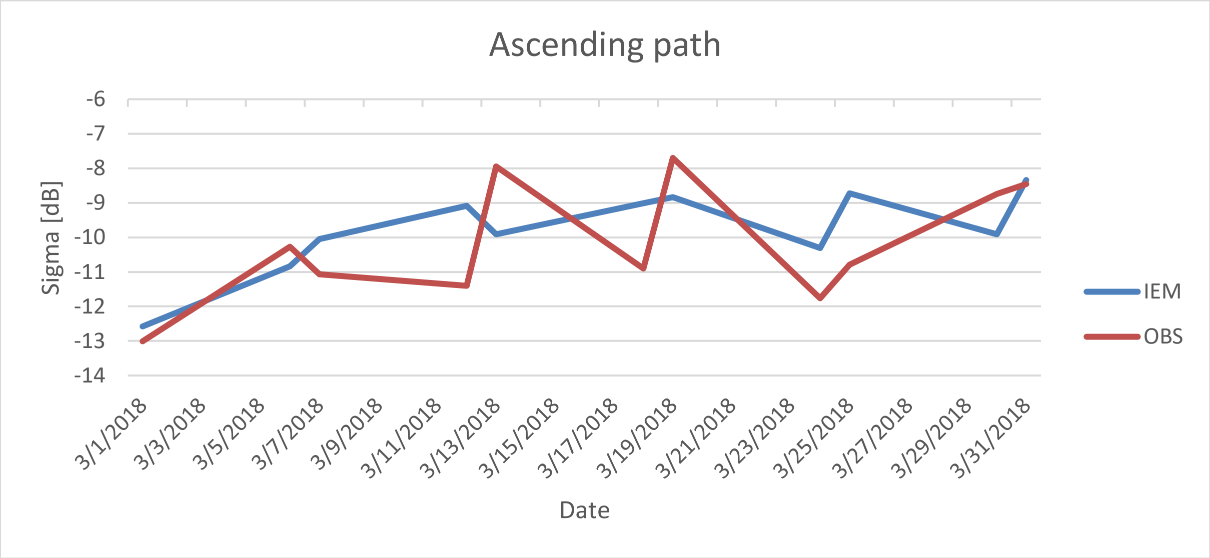

Figure 18 validated backscattering coefficients based on calibrated roughness parameters for ascending observations

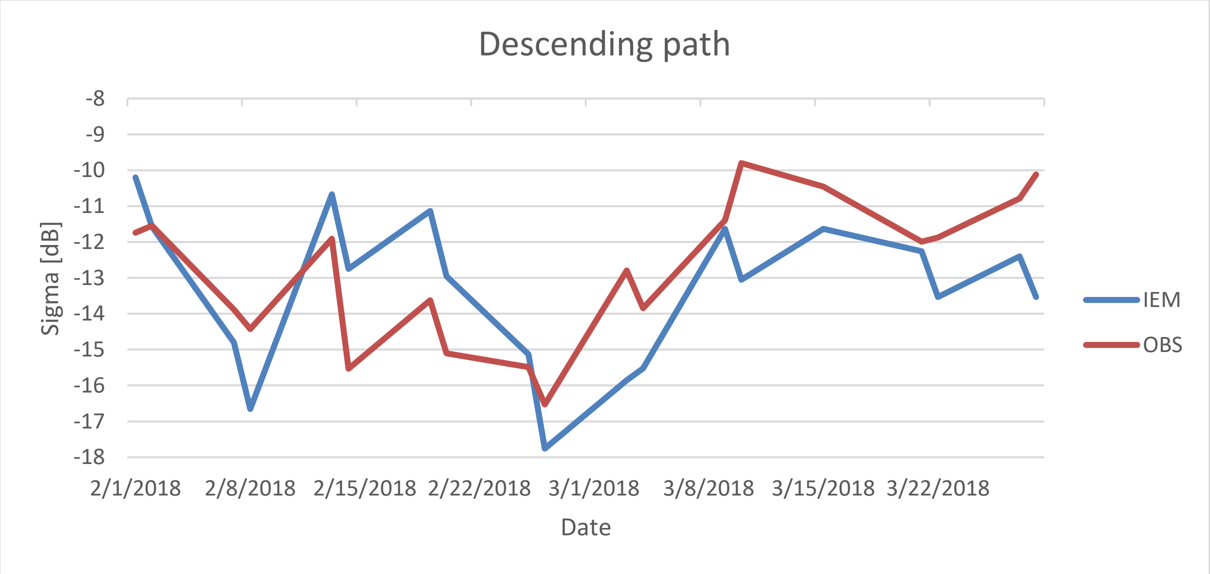

Figure 17 validated backscattering coefficients based on calibrated roughness parameters for descending observations

Moreover, the optimized roughness parameters were used to run the simulation and obtained the validation results for April, May, June, and July 2018 as significant vegetation growth is expected during this period, as shown in Figures 18 and 19. The obtained results show that as vegetation grows through April to July, the RMSE rapidly jumps to the unacceptable range, and IEM fails to estimate the backscattering observations accurately. It is observed that when the wheat field is developing, IEM consistently underestimates the backscattering values shown in table 12. This is due to vegetation scattering, which significantly increases the Sentinel-1 backscattering observations.

Table 12 obtained validation results in ascending and descending paths for April, May, June, and July 2018

Month	S2-NDVI-7	Ascending		Descending	
		RMSE [dB]	R	RMSE [dB]	R
18-Apr	0.18	1.66	0.73	3.73	0.52
18-May	0.26	1.73	0.69	3.51	0.93
18-Jun	0.32	2.25	0.21	5.47	0.28
18-Jul	0.6	5.17	0.34	8.65	0.33

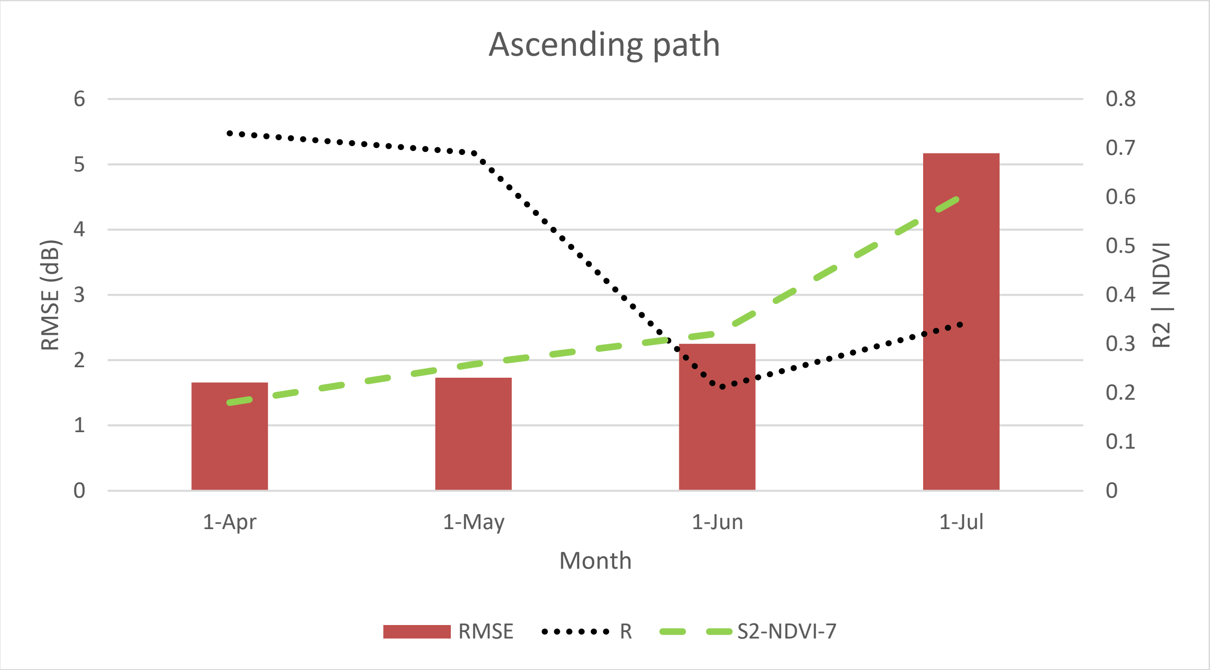

Figure 19 obtained validation results for April, May, June, and July, 2018 as significant vegetation growth is expected during this period for ascending path

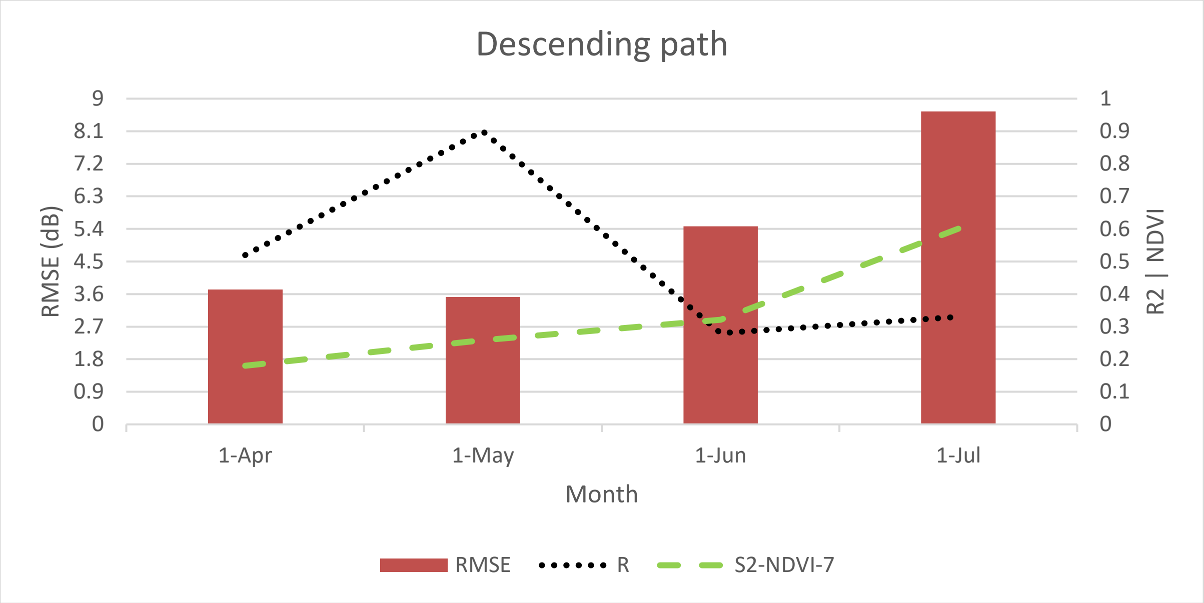

Figure 20 obtained validation results for April, May, June, and July, 2018 as significant vegetation growth is expected during this period for descending path

5.3. Calibration and validation of roughness parameters for the cornfield

According to figure 6, the TriplesSat image captured in August 2018 shows that the ground is plowed for a new crop. Therefore, it is necessary to recalibrate the roughness parameters as they lost their validity due to the tillage before planting the corn seeds. Again, the backscattering observations in August and September were divided into two parts to conduct a new calibration and validation process, as shown in table 13. The new recalibration process consequently results in the improvement of the WCM for the cornfield.

Table 13 present the dedicated validation and calibration periods for checking the optimization process in the cornfield

Paths	1-31th August 2018	1-15th September 2018
Ascending	**Calibration**	**Validation**
Descending	**Calibration**	**Validation**

5.3.1. The calibration process of roughness parameters for the cornfield

Recalibrating the roughness parameter for the corn period is a bit different from the previous section as the LoRa network at the northern farm field does not operate during the corn grow cycle and therefore captures no soil moisture value. As a result, we had to use ITCSM10 as the only available source of soil moisture data to replace with LoRa network. A comparison between different aggregated subsets of Sentinel-1 to obtain the best calibration results, as shown in table 12. In total, 21 backscattering observations (i.e. 10 Ascending, 11 Descending) was used to conduct the calibration process with similar procedure described in section 5.2.1.

Table 14 comparing the simulation results and observed backscattering observations at different spatial subsets

	Ascending path				Descending path			
subsets	s (cm)	l(cm)	RMSE (dB)	r	s (cm)	l (cm)	RMSE (dB)	r
10m	1.72	3	2.78	-0.14	1.47	19.8	2.01	-0.01
30m	0.92	10.8	2.1	-0.15	1.41	18.1	1.88	0.01
50m	1.04	13.9	1.77	-0.11	1.38	19.7	2.03	-0.09
70m	1.22	20	1.94	0.23	1.41	20	1.89	0.15
90m	1.1	19.9	1.04	0.47	1.19	15	1.45	0.43

According to table 14, comparing the different size of subsets, 90 by 90 m aggregated subsets shows the lowest RMSE and maximum r between the simulated results and backscattering observation from sentinel-1. A reason is that the 90 m subsets are representing the whole farmland as it was discussed previously in chapter 5.1.

5.3.2. Validation of roughness parameters for cornfield:

Assuming that in early September, the vegetation density is still negligible for backscattering observations, four ascending and descending observations between 1st and 15th September 2018 were selected to validate the obtained roughness parameter separately, as shown in table 15.

Table 15 comparing the IEM results and observed backscattering observations between 1st and 17th September 2018

Ascending	**Date**	**9/2/2018**	**9/3/2018**	**9/8/2018**	**9/9/2018**
	IEM	-10.33	-8.59	-11.13	-8.96
	OBS	-10.04	-8.01	-10.16	-10.12
Descending	**Date**	**9/5/2018**	**9/6/2018**	**9/12/2018**	**9/17/2018**
	IEM	-8.67	-10.38	-10.57	-10.15
	OBS	-9.79	-8.24	-10.33	-12.62

The backscattering observation was carefully selected from the 90-by-90 m subset, which is the area for which the highest correlation coefficient between the soil moisture and backscatter was found. The calibrated roughness parameters obtained are in an acceptable range, as shown in table 14.

Table 16 obtained validation results in ascending and descending paths in between 1st and 17th September 2018

Orbit path	s	l	RMSE	r
Ascending	1.1	19.9	0.82	0.66
Descending	1.19	15	1.73	0.52

5.4. Normalized Differential Vegetation Index (NDVI)

As described before, the NDVI values are a good indicator of vegetation water content. They can contribute to explaining the evolution of crop water content. Hence using the NDVI values should allow us to understand the spatial and temporal variation of vegetation water content and its relationship with the backscattering of Sentinel-1. The band four and band 7, were selected for calculating NDVI for monitoring vegetation water content at high spatial resolution (Darvishzadeh, Atzberger, Skidmore, & Schlerf, 2011).

Moreover, Comparing the daily variation of soil water content with derived NDVI from MODIS, Landsat-8, and Sentinel-2 is shown in figure 21. The calculated Pearson correlation coefficients between NDVI derived from MODIS and Landsat-8 with soil moisture data. The derived NDVI is associated with the area of northern farmland. Comparing calculated Pearson correlation coefficients between SM and sentinel-2 (0.42) with other non-commercial sensors, i.e., MODIS and Landsat-8 (ranging between 0.16 and 0.22, respectively), highlights the importance of Sentinel-2 for this study.

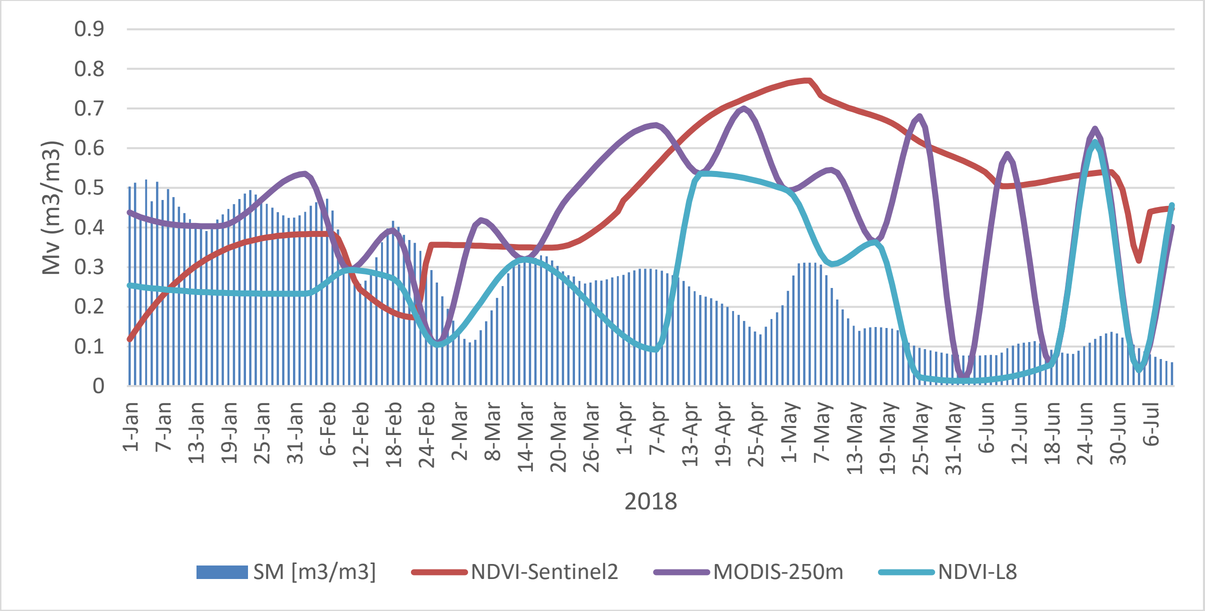

Figure 21 Compare the daily variation of soil water content with derived NDVI from MODIS, Landsat-8, and Sentinel-2

In addition, comparing the monthly average of NDVI at Northern farmland from Sentinel-2 different trends with two other NDVI products derived from MODIS and Landsat-8 is observed, as shown in figure 22.

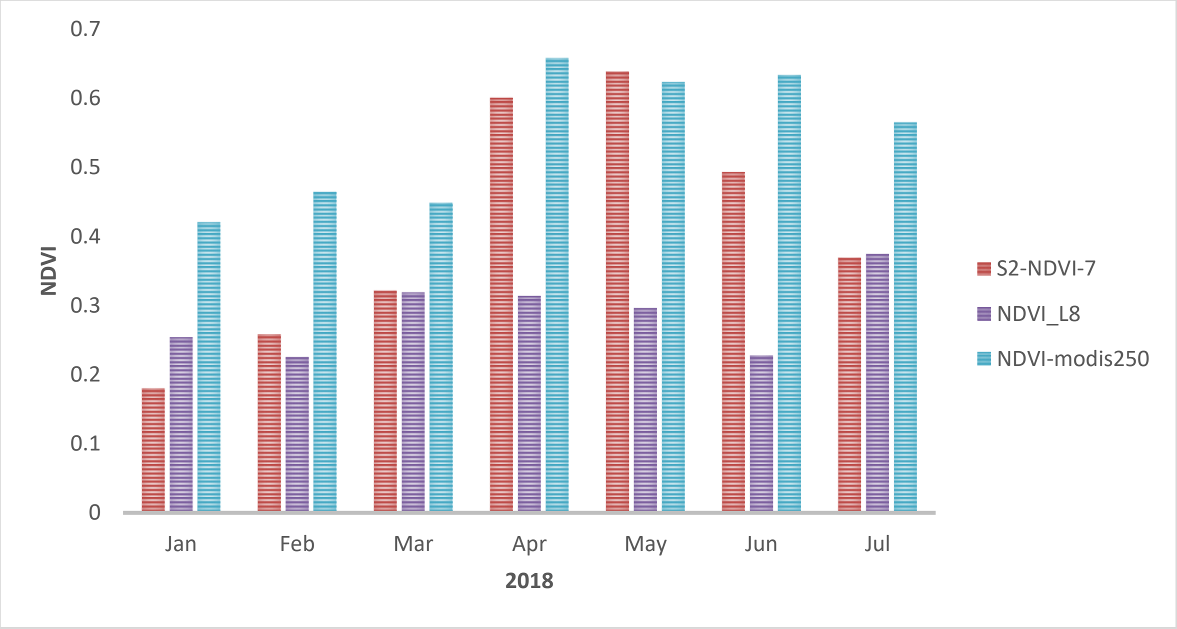

Figure 22 Compare the monthly average of NDVI products

To better understand the real trend of NDVI and realizing the actual situation at the northern farm field during this period, a sequence of high resolution (80 cm) panchromatic TripleSat images were collected. The TripleSat images present how the winter wheat had been growing month to month from March until harvesting time in August 2018. Due to fast growth between March and May, a significant increase of NDVI from March to the pick of the growth cycle in May was expected. However, the obtained NDVI values from Landsat-8 did not respond to this rapid growth appropriately, while the obtained NDVI from Sentinel-2 increased dramatically. Moreover, due to the ripping of the winter wheat in June and July, the color of winter wheat changed to goldish color. As a result, the obtained NDVI values in July start to decrease as they were observed in obtained NVDI from Sentinel-2. On the other hand, the obtained NDVI from MODIS is constantly higher than it was expected, which could be due to the coarse spatial resolution of MODIS, which is affected by the landcover in adjacent areas. The obtained NDVI values from Sentinel-2 is seen to be the best match with the vegetation condition at northern farmland, as shown in figure 23.

Figure 23 The images from Triple-Sat demonstrate the growing cycle of winter wheat from March to September, 2018. Source: The Netherlands Space Office (https://www.spaceoffice.nl/nl/satellietdataportaal/beschikbare-data/uitleg-data/product-levels/)

5.5. Assessment of Harmonic Analysis of Time Series (HANTS) for NDVI

The revisiting time of sentinel-1 is every three days on average, which is much higher than the revising time of Sentinel-2 in every four to five days. In addition, due to the atmospheric conditions in the Netherlands, 65% of days is a cloudy day cite. As a result, in the best-case scenario, there will be a smaller number of observations captured by Sentinel-2 comparing to the obtained backscattering values from Sentinel-1.

Out of 49 observations, only 32 valid estimated NDVI values were obtained from S2L2 observations in the entire year of 2018, while over 240 observations were obtained sentinel-1 for the same period. Different interpolation techniques (i.e. Harmonic Analysis of Time Series (HANTS) algorithm Verhoef (2000), and the piecewise linear function) were used to fill the gaps and estimate NDVI values at missing dates.

A big challenge to assess the impact of interpolation techniques is that the crop factors are calibrated based on the given NDVI values. Crop factors are particular to the given NDVI values since the NDVI has a huge influence on calibrating the crop factors (*A, B*). As a result, it is important to assess the estimated NDVI values and the impact of the interpolation technique on the obtained simulation results. Therefore, any changes in the estimated NDVI values will no longer support the calibrated crop factors and increase the obtained RMSE. Therefore, the crop factors were recalibrated through an iteration process in which different HANTS-derived NDVI values with the different number of frequencies (nf) are being used to estimate a new crop factor.

The iterative simulation re-calibrates the crop factors for both ascending and descending paths. The observations were divided into two periods from 1st April to the end of June and from 1st of August until the end of December for wheat and corn, respectively.

The range and the initial values to obtain the optimized value were found widely different. The obtained optimized crop factor values for A was at a range between 30 and 300, while the B factor range was a range between 0.01 and 0.09 with 0.01 divisions.

The evolution of HANTS is beyond the scope of this study; however, we conduct a preliminary assessment between HANTS and the piecewise linear function. The obtained results show that HANTS is not performing well to interpolate the NDVI values as it does not preserve the actual values of NDVI at the given dates, which will add more complications to the simulation process. As a result, we selected the piecewise linear function that simply follows the trend of NDVI values in a piecewise way and preserves the values close to the actual observations.

5.6. Optimizing crop factors for winter wheat

According to table 17, comparing the optimized crop factor between ascending and descending observations shows a significant difference between them. The soil moisture changes and the variation of the canopy have been involved in the optimization process, and both variables are used as inputs to run the simulation for both ascending and descending observations.

Table 17 The estimated values of crop factor for winter wheat on April, May, June, and July, 2018

	Ascending					**Descending**			
Wheat	**Month**	**A**	**B**	**RMSE (dB)**	**R (%)**	**A**	**B**	**RMSE (dB)**	**R (%)**
	1-Apr-18	-0.1	-0.01	1.65	0.73	-43	-0.001	2.34	0.34
	1-May-18	-0.1	-0.01	0.62	0.90	-27	-0.001	1.61	0.91
	1-Jun-18	-0.4	-0.01	1.3	0.21	-66	-0.001	1.52	0.10
	1-Jul-18	-4.3	-0.08	0.99	0.20	-300.6	-0.001	1.66	0.36
	Overall	-0.2	-0.06	1.69	0.71	-43	-0.001	2.1	0.53

Taking to account that the B factor contribute in the attenuation process of vegetation, it is concluded that winter wheat has much more attenuation effect at descending observations in comparison with ascending observations. Consequently, The B factor at the descending path has become almost one-tenth of B factor for ascending observations. This means that the attenuation for ascending observations is one-tenth of the descending path.

In the context of uncertainty, this could be a result of soil moisture variation during the day when the morning passes vegetation has more water than in the afternoon as soil moisture is averaged in a daily basis, and it is not clear whether this is the case or not. However, this could also be related to the scattering configuration of the wheat field. According to Picard, Le Toan, & Mattia, (2003), the V-polarized signals interact more than the H-polarized signal with the vertical stems, generating higher-order attenuation effects. As a result, the V-polarized signals attenuate more than H-polarized signals at the vertical stems, and with the rise of stem height, the attenuation slightly rises. Similar to H-polarized signals, the descending observations of sentinel-1 has obtained more attenuation. In fact, the obtained backscattering observations from the descending path behave exactly similar to the H-polarized signals, which is reasonable because the direction of v-polarized backscattering at the descending path is actually oriented horizontally to the wheat field. Similarly, it is observed that the A factor in descending observation is almost ten times higher than ascending observations, which is a result of lower scattering effect of H-polarized observations. Therefore, the crop factors are playing crucial roles in determining the amount of scattering and attenuation processes for ascending and descending observations.

Figure 24 overview of estimated total backscattering value and backscattering observations for winter wheat

.

According to figure 23, the obtained results in a stepwise growing development show that IEM is not able to properly describe the attenuation process inside the wheat field at ascending and descending observations. However, with an increase of stem density and crop height, the RMSE decreases from a few decibels to tens of decibels.

Moreover, the WCM scattering process (A) are less significant at ascending observations as the new crop coefficients in ascending observations are much smaller comparing to descending observations. The WCM attenuation process varies in a similar way compared to the attenuation effect of IEM due to the variation of vegetation water content and crop height. However, it is not clear to what extend the crop density is contributing to the attenuation process as we do not have this parameter to measure the effect properly. It is highly expectable that the attenuation is only indirectly related to crop biomass. If the attenuation process is the leading factor, it is possible to estimate the wheat biomass of a given area since the crop density usually remains constant during different stages of developing crops. However, this is highly variable in different farm fields. As a result, the attenuation effect varies from a wheat field to another wheat field (Picard et al., 2003).

By comparing the obtained figure at different stages of wheat development, three essential points can be drawn.

1) The IEM is in substantial disagreement with the VV polarization data from the initial stage to the development stage, e.g., when the wheat is well ripening.
2) The WCM is in better agreement with the VV polarization data than the IEM.
3) The difference between the WCM and the backscattering observations depends on the vegetation water content and the direction of observations (i.e., ascending or descending).

5.7. Optimizing crop factors for Cornfield

It takes roughly 60 days that corn stalk reaches to the maximum developed stage around 2.4 m height. In a further step, the WCM model was developed for cornfield (Hosseini et al, 2015). The interaction mechanisms are slightly different for cornfield as the interaction between soil and corn is not predictable at different stages of corn development, as is shown in table 24 and 25. The estimated A factor in table 18 start to rise from -1.2 to -0.1 as the cornfield start to grow. This indicates that the scattering effect in corn has been slightly increased. At the same time, the B factor slowly decreases, which indicates that the attenuation process slowly decreases. Therefore, we can conclude that when the corn is at the initial stages of development, the attenuation is high. As the corn reaches advanced stages, the scattering process will be dominant. This should be related to the height of corn stem in which the size of vegetation is actually beyond the tolerance to pass through the vegetation canopy and reach the ground surface.

Table 18 shows the estimated values of crop factor for ascending observations of Sentinel-1 in a cornfield

	Ascending						
Corn	**Month**	**A**	**B**	**RMSE WCM (dB)**	**RMSE IEM (dB)**	**R_WCM**	**R_IEM**
	1-Sep-18	-1.2	-0.05	0.792	1.126	0.71	0.73
	1-Oct-18	-1.1	-0.03	1.356	1.684	0.15	0.29
	1-Nov-18	-0.1	-0.09	1.02	2.249	0.11	0.42
	Overall	-0.5	-0.06	1.536	1.715	0.43	0.46

Table 19 The estimated values of crop factor for descending observations of Sentinel-1 in corn field

	Descending						
Corn	**Month**	**A**	**B**	**RMSEWCM (dB)**	**RMSEIEM (dB)**	**R_WCM**	**R_IEM**
	1-Sep-18	-0.7	0.61	0.002	2.508	-0.16	-0.25
	1-Oct-18	-2	0.1	0.006	1.785	-0.49	0.3
	1-Nov-18	-8.6	0.03	0.004	3.401	-0.06	0.14
	Overall	-0.8	0.32	0	2.67	-0.14	0.07

Moreover, the obtained simulation results via the IEM overestimate the backscattering observation obtained during the ascending view during September and October 2018, while the calculated backscattering coefficient becomes hugely underestimated in November 2018. Therefore, developing crop coefficients for cornfield seems to have more uncertainties.

According to figure 25, it was observed that the scattering process is the dominant factor that affects IEM simulation by 2.4 dB in the stages of the growing cycle in the cornfield. The obtained results show that the RMSE of IEM varies from 1.7 to 3.4 dB. Consequently, with the growth of corn height, the RMSE of IEM jumps rapidly. As a result, compared to the backscattering observations from sentinel-1 is not able to adequately describe the scattering process inside the cornfield at ascending and descending observation.

The WCM scattering process varies similarly compared to the scattering effect of IEM due to the variation of vegetation water content and crop height. However, due to the fixed structure that is used in the model, a complete breakdown of the backscatter is not possible (Picard et al., 2003). Nevertheless, to realize the comparative influence between soil and the backscatter that is resulted from corn–soil interactions, it is very imperative to calculate the sensitivity of the total backscatter to soil parameters. For this reason, a set of simulations using WCM with different vegetation interface was carried out. The results indicate that the backscatter at the different vegetation developing stages are extremely diverse at ascending and descending observations.

As a result, the total backscatter that originates from the soil surface is attenuated by the corn and the interactions between the corn and the soil surface. A comparative involvement of these two interactions depends on different vegetation developing stages and the direction of orbit.

Moreover, the vegetation effects are more significant at descending observations. Consequently, the WCM seems to give better results compared to the IEM. In the context of uncertainty, this is mainly because the IEM underestimates the attenuation effect since corns are supposed to be strictly vertical. However, this is just a presumption because the WCM does not consider the leaves size. On the other hand, the IEM overestimates the backscatter because the corn attenuation is underestimated. The key parameter that is limiting both models is a lack of information about the leaves factor. The estimated values of crop factor for ascending and descending observations of Sentinel-1 in a corn field is shown in figures 24 and 25, respectively.

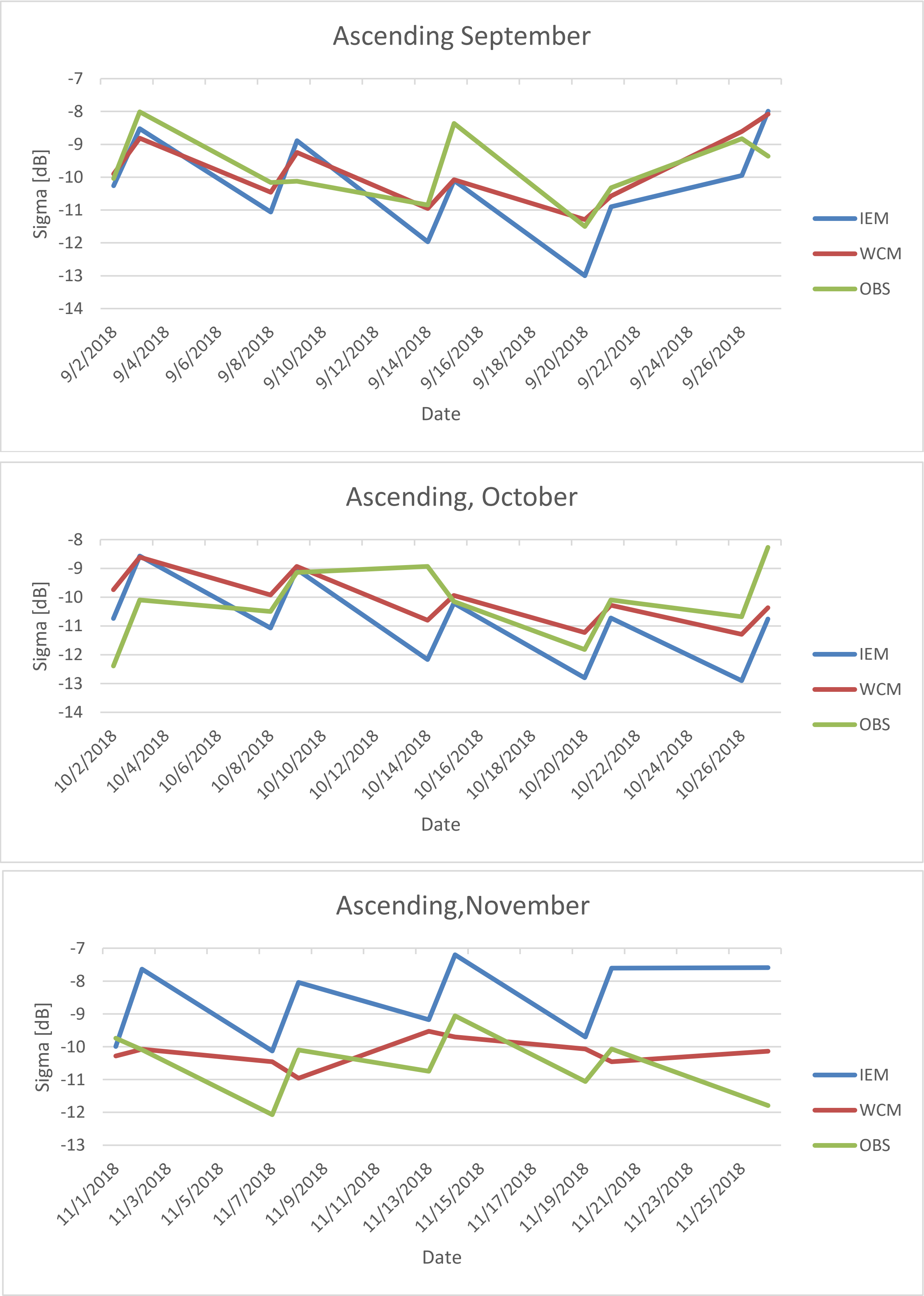

Figure 25 compares the total backscattering value and ascending observations of Sentinel-1 in the cornfield

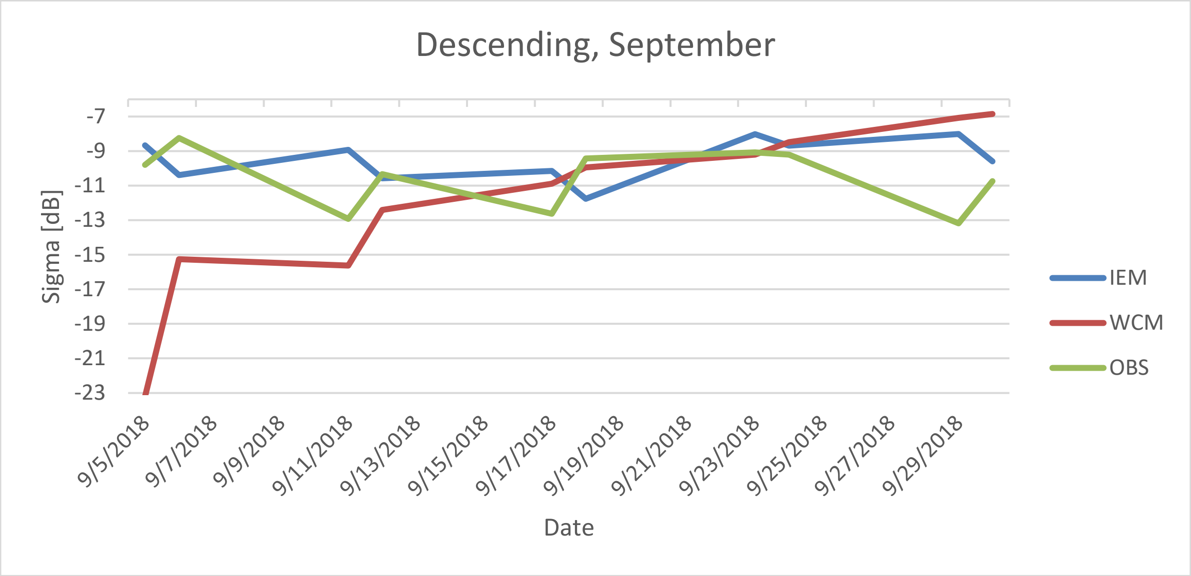

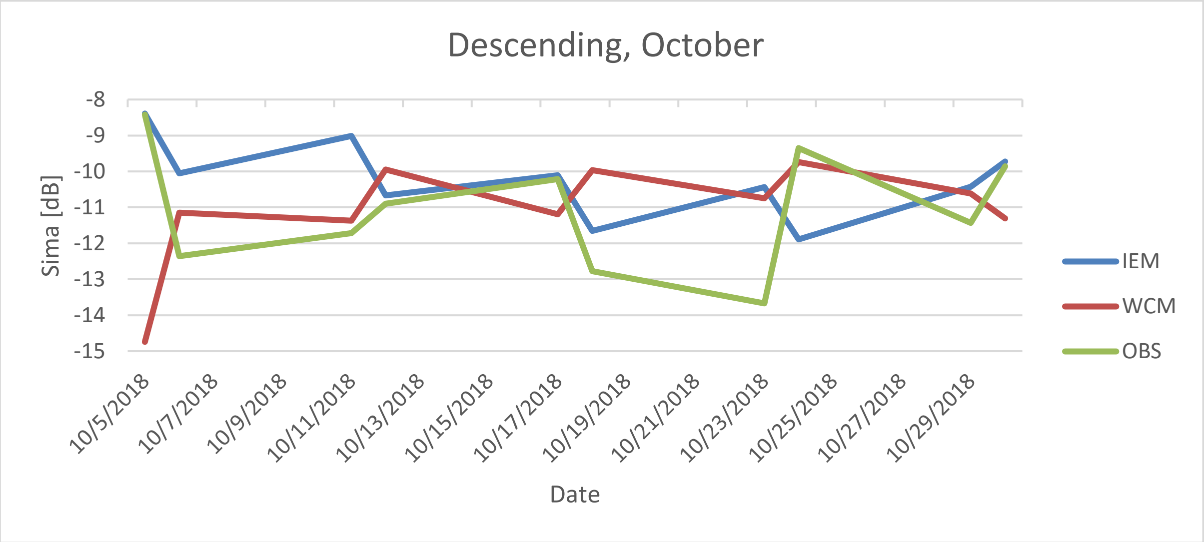

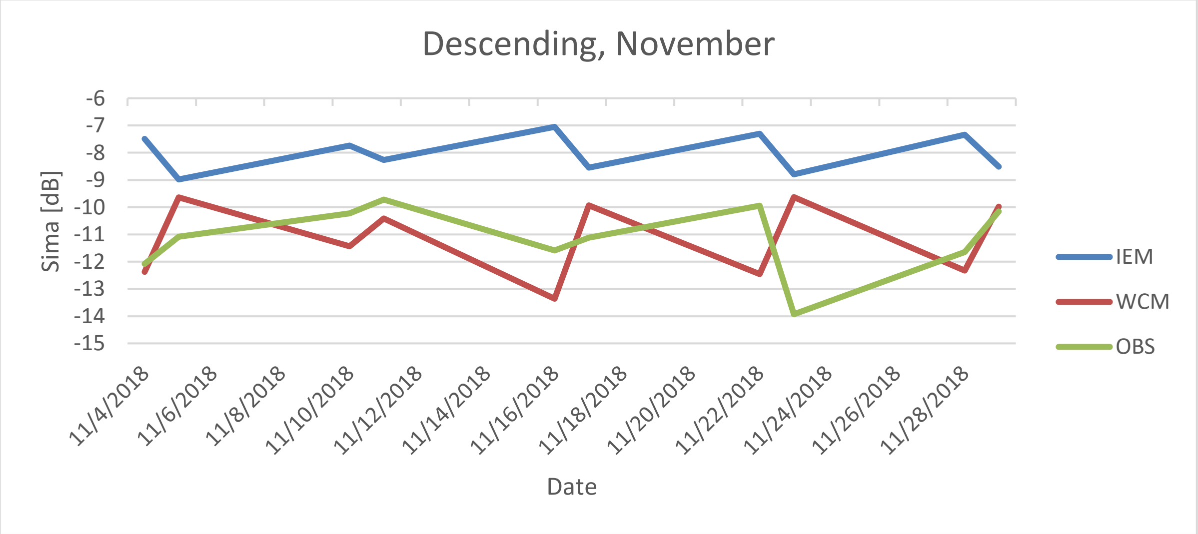

Figure 26 compares the total backscattering value and descending observations of Sentinel-1 in the cornfield

5.8. Effect of Surface Parameters on Backscattering observations in IEM

According to figure 26, there is an exponential relationship between backscattering observation and soil water content. The exponential relationship between backscattering observation and dielectric constant is estimated based on the given roughness parameters and crop factors at corn and wheat fields. When soil-water content is low, the backscatter observations are highly sensitive to the variation of soil moisture. As the soil moisture content increases, the backscatter observations become almost insensitive to the soil moisture. Moreover, the backscatter observations are lower for high roughness parameters, relating to an increase in scattering effect.

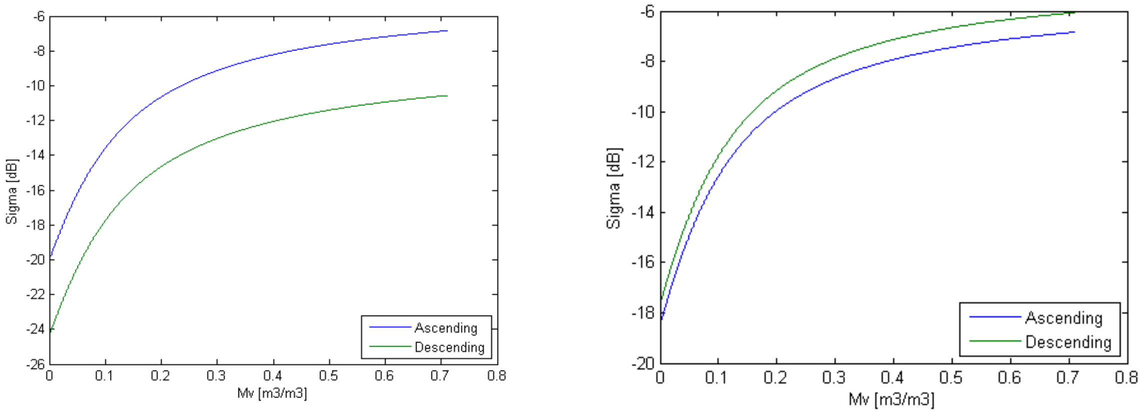

Figure 27 shows the effect of surface parameters on the backscattering coefficient in IEM for the wheat field (on the left), and cornfield.

5.9. Retrieving soil moisture

Retrieving soil moisture in corn and wheat fields requires two steps: the first step is to remove the effect of vegetation, and the second step is to validate the retrieved Soil moisture via ground measurements.

5.9.1. Removing vegetation effect

It was discussed, IEM is mostly affected by the attenuation process at the wheat field, while it is mostly dominated by the scattering process through the cornfield. Moreover, linking between the backscattering signals and vegetation properties by using a multi-scattering model, i.e., WCM at different subsets. The monthly training process developed new crop factor coefficients for each month, which can be used to remove vegetation effect and retrieve soil moisture more accurately than the surface scattering model, IEM. However, the obtained crop factors require to be tested and validated against ground measurements. The validation process was carried out by comparing the retrieved soil moisture with ground measurements from LoRa networks.

Since there is several ground stations across the farm field via the LoRa network, we were able to carry out the validation for different subsets and evaluate the results spatially. In that case, the collected backscattering observations at one instant (e.g., a day) are used to create a daily soil moisture product. The validation process is carried out for wheat and corn at 50 m and 90 subsets, respectively. Moreover, It would be interesting to know the extent of what will be the maximum testing capacity of the newly developed WCM and to conclude what subset has the best performance among all the other subsets. The ground measurements from the LoRa network, as well as the footprint of retrieved soil moisture at different subsets, are presented in figures 27-29.

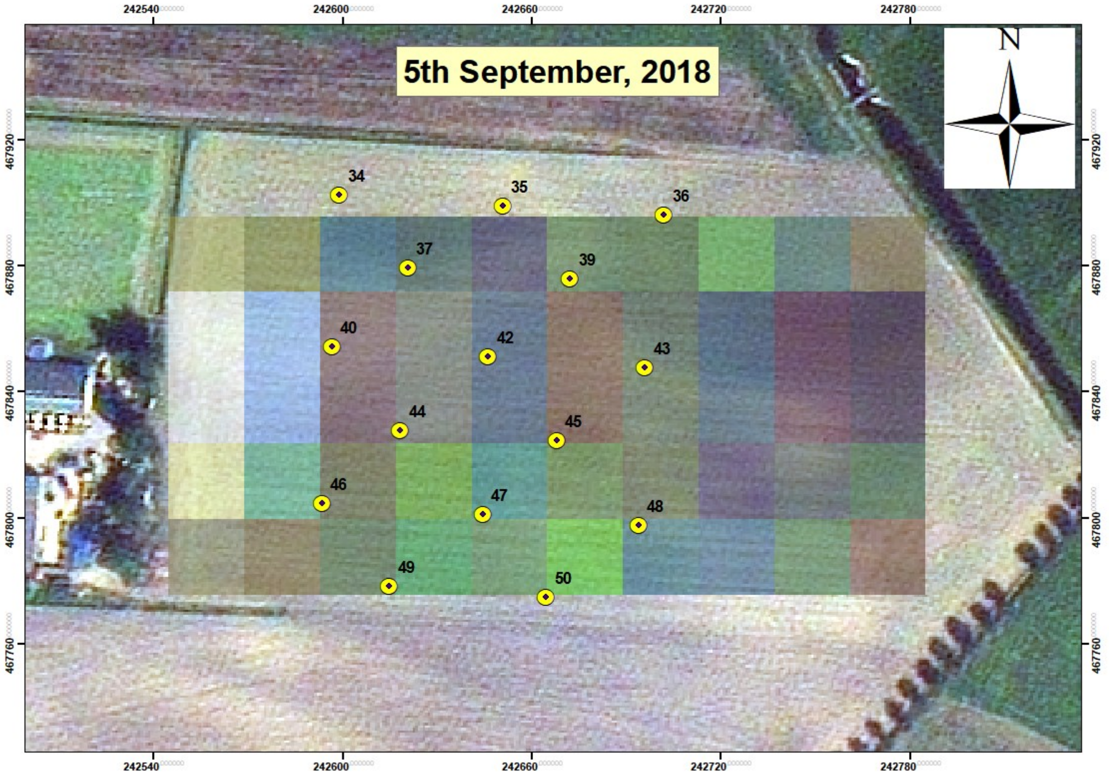

Figure 29 footprint of Sentinel-1 backscatter observations at 10m subset via GEE along with the underlying TripleSat image captured on 5, September, 2018

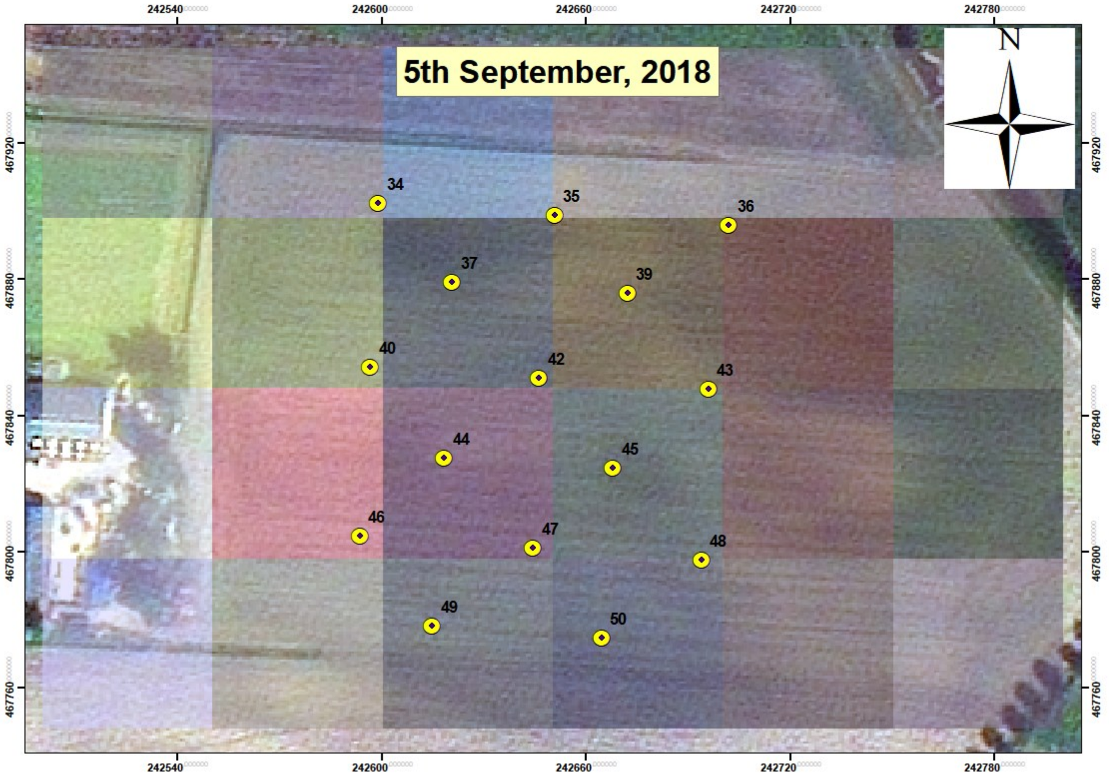

Figure 28 footprint of sentinel-1 backscatter observations at 50m subset via GEE along with the underlying TripleSat image captured on 5, September, 2018

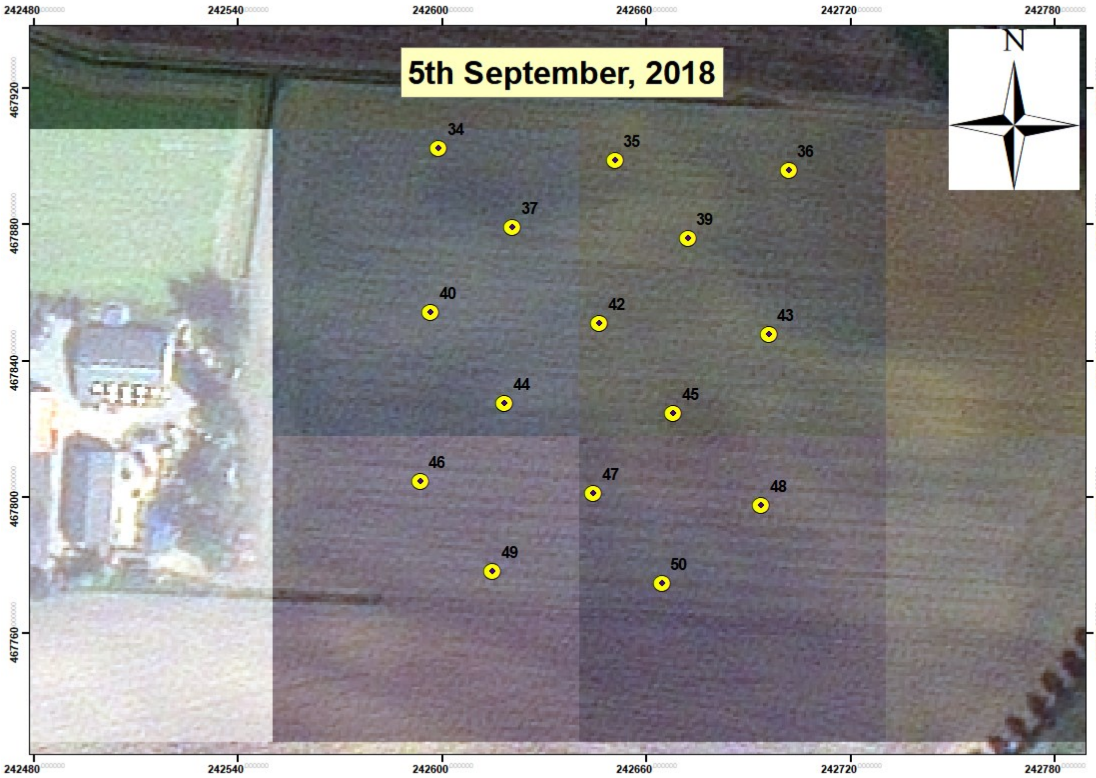

Figure 30 footprint of sentinel-1 backscatter observations at 90m subset via GEE along with the underlying TripleSat image captured on 5, September, 2018

5.9.2. Scene-based Soil moisture validation

The soil moisture values are validated via RMSE function between the ground soil moisture measurements and the retrieved soil moisture.

To investigate the accuracy of obtained results, a series of images from Sentinel-1 were collected. The collected images were evenly distributed through the wheat period in 2018. Table 20, shows the dates of collected images.

Table 20 list of collected images for validation of retrieved soil moisture during the wheat growing cycle via GEE

	Date	Theta (degree)	NDVI	Ascending	Descending
1	3 May 2018	41.15	Sentinel-2	-	Sentinel-1
2	6 May 2018	37.38	Sentinel-2	Sentinel-1	-
3	8 May 2018	41.15	Sentinel-2	-	Sentinel-1
4	11 May 2018	37.38	Sentinel-2	Sentinel-1	-
5	15 May 2018	41.15	Interpolated	-	Sentinel-1
6	4 June 2018	37.38	Interpolated	Sentinel-1	-
7	8 June 2018	41.15	Interpolated	-	Sentinel-1
8	11 June 2018	37.38	Interpolated	Sentinel-1	-
9	13 June 2018	41.15	Interpolated	-	Sentinel-1
10	5 July 2018	37.38	Sentinel-2	Sentinel-1	-
11	7 July 2018	41.15	Sentinel-2	-	Sentinel-1
12	10 July 2018	37.38	Interpolated	Sentinel-1	-

According to table 21, the obtained results from retrieved soil moisture in wheat field was compared with twelve ground stations across the wheat field. The obtained results show consistent accuracy along the growing cycle of wheat. A slight increase of RMSE above 0.1 (m3/m3) was observed at the end of May and early of June which should be as a result of heterogeneity in the land cover during this period.

Table 21 show the accuracy of Scene-based retrieved soil moisture during the wheat growing cycle

	Date	RMSE (m3/m3)	R
1	**3 May 2018**	0.13	0.08
2	**6 May 2018**	0.1	-0.34
3	**8 May 2018**	0.04	0.05
4	**11 May 2018**	0.15	-0.35
5	**15 May 2018**	0.03	0.09
6	**18 May 2018**	0.15	-0.17
7	**4 June 2018**	0.12	0.06
8	**8 June 2018**	0.08	0.12
9	**11 June 2018**	0.07	0.13
10	**13 June 2018**	0.10	0.17
11	**16 June 2018**	0.08	0.01
12	**5 July 2018**	0.11	0.20
13	**7 July 2018**	0.09	0.01
14	**10 July 2018**	0.12	0.12

5.9.3. Time series Soil moisture validation

According to table 22, the retrieved soil moisture for ascending observations in wheat field shows 0.09 (m3/m3) RMSE error against ground measurements at 50-meter aggregated subset. On the other hand, retrieved soil moisture for or ascending observations in wheat field shows a significant 0.2 (m3/m3) RMSE error against ground measurements. The obtained results do not show a consistent accuracy between the ascending and descending observation during the growing cycle of wheat.

Moreover, the retrieved soil moisture in corn field shows 0.14 and 0.13 (m3/m3) RMSE error against ground measurements for ascending and descending observations, respectively. The retrieved soil moisture uses 90-meter aggregated subset the obtained results show a consistent accuracy between the ascending and descending observation during the growing cycle of corn.

Table 22 show the accuracy of Time series retrieved soil moisture during the wheat and corn growing cycle

	Date	RMSE (m3/m3)	R2
1	**Ascending Wheat**	0.09	0.46
2	**Descending Wheat**	0.2	0.31
3	**Ascending corn**	0.14	0.31
4	**Descending Corn**	0.13	0.19

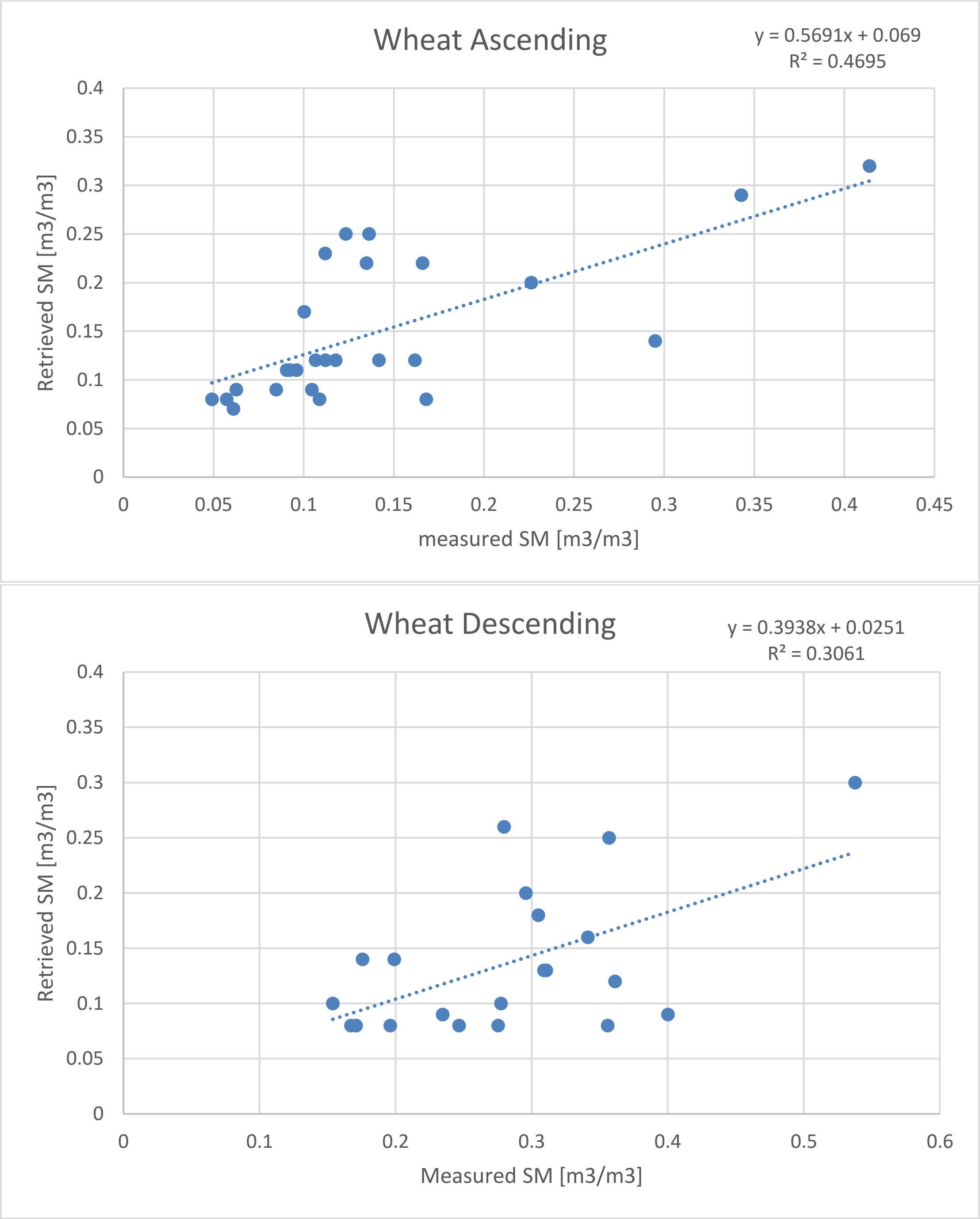

Figure 31 show the retrieved soil moisture against the soil moisture measurements for ascending and descending observations during Wheat grow cycle

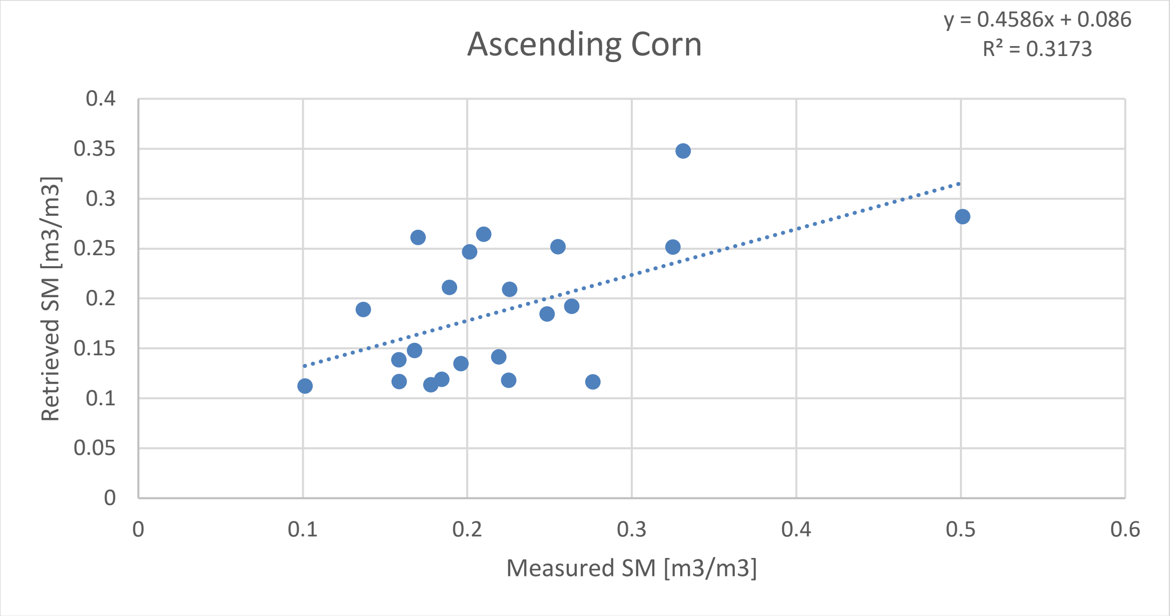

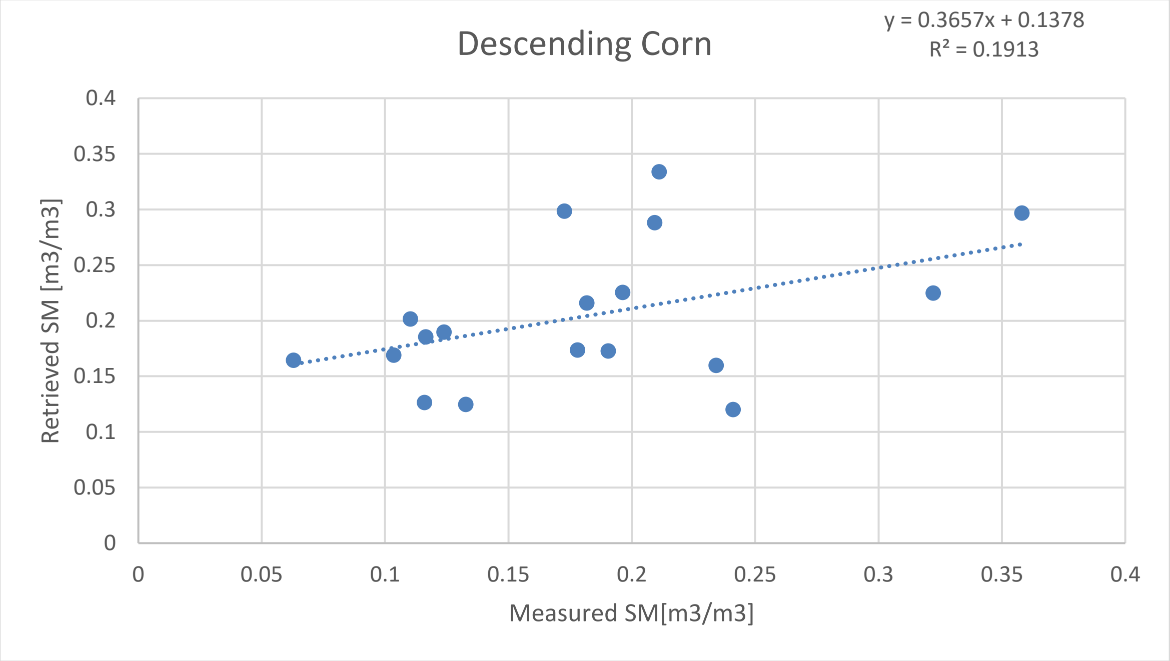

Figure 32 show the retrieved soil moisture against the soil moisture measurements for ascending and descending observations during corn grow cycle

6. IMPLEMENTATION OF GEE-BASED SOIL MOISTURE RETRIEVAL (SMR) PLATFORM

6.1. Introduction

This section describes the conceptual framework of GEE-based soil moisture retrieval (SMR) platform. Although all the processing at this study is originally conducted via compiling Fortran with Matlab, from day one, part of the plan was to develop a GEE-based SMR platform. Currently, the initial steps of data collection and processing consist of the heavy data management. The image pre-processing of sentinel-1 and 2 are conducted via the help of GEE which otherwise this study would not be possible to take place.

6.2. Technical Requirments

GEE use a set of interoperable middleware web applications that interface with the database back–end and deliver the maps for visualization purposes. The design of the GEE is a simple browser-based platform that allows clients to easily access the product. The design of the GEE Geo-webservice is presented in figure 33.

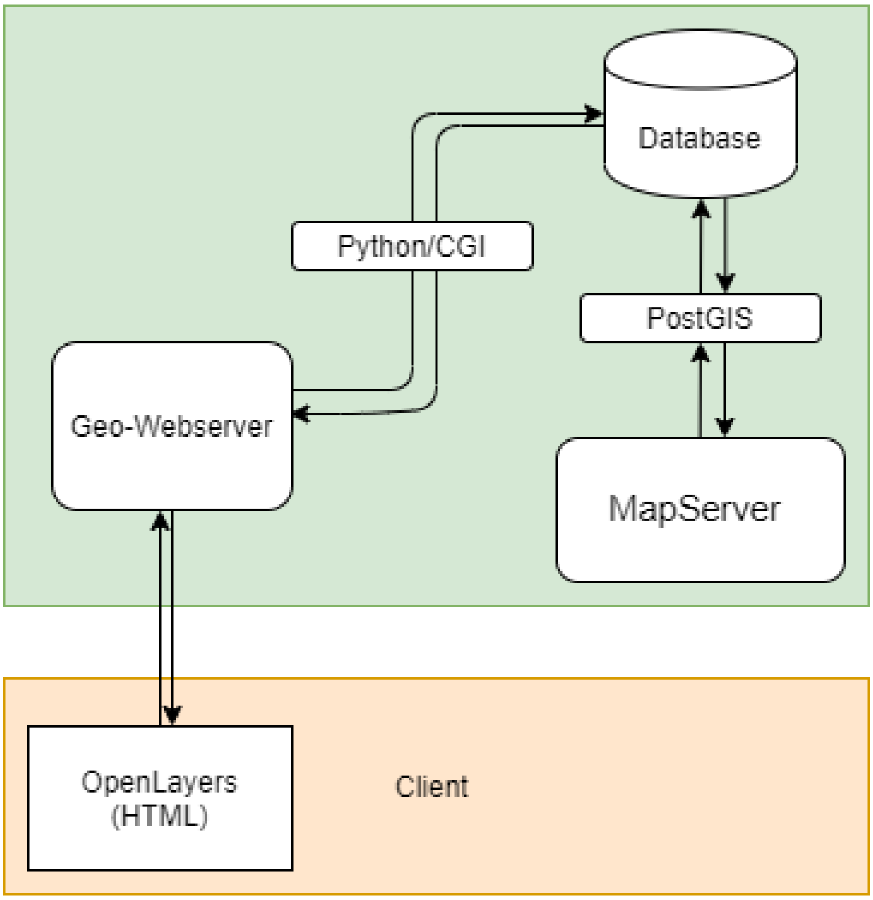

Figure 33 the design of GEE web service source

6.2.1. Image collection

SMR requires to collect Sentinel-1 and 2 images daily and a set of parameters to keep the process moving forward. The data collection requires to represent a consistent observation through time. The collected data product used in this study is expressed as below:

ee.ImageCollection('COPERNICUS/S1_GRD')
ee.ImageCollection('COPERNICUS/S2')

The collected data from sentinel-1 should be filtered out via the filtering functions. The collected images from sentinel-2 should be free of atmospheric errors, clouds and shadows. The daily basis variation in a time series is expected to be only the outcome of the physical change in land surface. For instance, the API functions used at this platform follow the same procedure as was used for sections 3.1 and 3.2.

The collected images from Sentinel-2 are expected to be once every seven days. However, due to masking out the clouds a significant number of observations are reduced. As a result, the best way to retrieve the vegetation index is to use the nearest observation targeting as the same day as the crop cycle is not fast enough to change within a few days.

Note that within the API some functions are provided to calculate the vegetation index and convert them to a collection of daily basis format to be used as an input for SMR.

6.3. Running SMR

There are different approaches to operate the API including: Calling methods within the objects, calling algorithms, Calling Code Editor, and implementing new functions. SMR runs through Code Editor which is defined at a root dictionary in GEE account.

To describe how SMR run in GEE Code Editor, it should be broken down into 3 steps. The following snippets show the steps that has to take place to collect, process and store the output. These snippets are only to give an insight of what is happening inside the SMR. The SMR is a collection of all of these piece of API functions that runs together.

Describing the starting and ending dates of the times series:

```
var startingdate = '2018-05-01';
var endingdate   = '2018-12-30';
```

Defining a region of interest (roi) to run SMR using ee.Geometry function

```
var roi = ee.Geometry.Polygon(
        [[[6.6676,  52.19120],
          [6.6676,  52.19235],
          [6.6710,  52.19235],
          [6.6710,  52.19120]]], null, false);
```

Providing the required parameters via the parameters is shown below:

```
var parameter = {
  rms height:             0.39,
  lengthfunction:          3,
  A_ascending_wheat:   -0.2,
 B_ascending_wheat:   -0.06,
};
```

Collecting sentinel-1 images and subsetting the selected bands:

```
var imgVV = ee.ImageCollection('COPERNICUS/S1_GRD')
        .filterBounds(roi)
        .filterDate(startingdate, endingdate)
```

```
.filter(ee.Filter.listContains('transmitterReceiverPolarisation',
'VV'))
        .filter(ee.Filter.eq('instrumentMode', 'IW'))
        .map(function(image) {
          var edge = image.lt(-30.0);
          var maskedImage = image.mask().and(edge.not());
          return image.updateMask(maskedImage);
        });

};
```

Filtering the ascending and descending observationsas well as the incident angles to run SMR at root dictionary:

```
var desc = imgVV.filter(ee.Filter.eq('orbitProperties_pass',
'DESCENDING')).select('VV');
print(desc,'desc')
var asc = imgVV.filter(ee.Filter.eq('orbitProperties_pass',
'ASCENDING')).select('VV');
print('asc',asc)
var tetadesc = imgVV.filter(ee.Filter.eq('orbitProperties_pass',
'DESCENDING')).select('angle');
var tetaasc = imgVV.filter(ee.Filter.eq('orbitProperties_pass',
'ASCENDING')).select('angle');
```

Masking the clouds built-in function:

```
function maskS2clouds(image) {
  var qa = image.select('QA60');

  // Bits 10 and 11 are clouds and cirrus, respectively.
  var cloudBitMask = 1 << 10;
  var cirrusBitMask = 1 << 11;

  // Both flags should be set to zero, indicating clear
conditions.
  var mask = qa.bitwiseAnd(cloudBitMask).eq(0)
      .and(qa.bitwiseAnd(cirrusBitMask).eq(0));
      return image.updateMask(mask).divide(10000);
}
```

Collecting Sentinel-2 images and vegetation index. The vegetation index is also included as an additional band as below:

```
var s2 = ee.ImageCollection('COPERNICUS/S2')
                  .filterBounds(roi)
                  .filterDate(startingdate, endingdate)
// Pre-filter to get less cloudy granules.
        .filter(ee.Filter.lt('CLOUDY_PIXEL_PERCENTAGE', 20))
         .select('B[4-8]')
// This function adds the ndvi index band to the Sentinel-2
images.
var addNDVI = function(image) {
  return image
    .addBands(image.normalizedDifference(['B7',
'B4']).rename('NDVI'))
```

```
    //.addBands(image.metadata('system:time_start'));
```

It is very difficult to get observations from both satellites at the same time. Filtering the collected data based on date allow us to make segments in time and export only the specified date as below:

```
var spring = ee.Filter.date('2018-05-1','2018-05-7');
//print (spring,'spring');
var lateSpring = ee.Filter.date('2018-05-8','2018-05-14');
//print (lateSpring,'lateSpring');
var summer = ee.Filter.date('2018-05-15','2018-05-22');
```

Assembling the bands into one file:

```
// sigma
var descChange = ee.Image.cat(
        desc.filter(spring).mean(),
        desc.filter(lateSpring).mean(),
        desc.filter(summer).mean());
var ascChange = ee.Image.cat(
        asc.filter(spring).mean(),
        asc.filter(lateSpring).mean(),
        asc.filter(summer).mean());
// incident angle
var tetadesc = ee.Image.cat(
        tetadesc.filter(spring).mean(),
        tetadesc.filter(lateSpring).mean(),
        tetadesc.filter(summer).mean());

var tetaasc = ee.Image.cat(
        tetaasc.filter(spring).mean(),
        tetaasc.filter(lateSpring).mean(),
        tetaasc.filter(summer).mean());
// Compute NDVI
var ndviS21 = s2
  .map(addNDVI)
  .select('NDVI')
  .filter(spring).mean();
var ndviS22 = s2
  .map(addNDVI)
  .select('NDVI')
  .filter(lateSpring).mean();
var ndviS23 = s2
  .map(addNDVI)
  .select('NDVI')
  .filter(summer).mean();
ndviS2=ee.Image.cat(ndviS21,ndviS22,ndviS23);
var ndviS2=ndviS2.clip(roi);
```

Reprojection from geographic coordinate system (WGS84) to the local dutch coordinate system (RD_NEW):

```
var reprojecteds2 = ndviS2
    .reproject('EPSG:28992', null, 50);
var reprojectedasc = imgasc
    .reproject('EPSG:28992', null, 12.50);
var reprojecteddesc = imgdesc
    .reproject('EPSG:28992', null, 50);
```

Exporting the data is done via the following scripts:

```
// Export the image, specifying scale and region.
Export.image.toDrive({
  image: reprojecteds2,
  description: 'ndviS2',
  scale: 50,
  region: roi
});
Export.image.toDrive({
  image: reprojectedasc,
  description: 'imgasc',
  scale: 50,
  region: roi
});
Export.image.toDrive({
  image: reprojecteddesc,
  description: 'imgdesc',
  scale: 50,
  region: roi
});
Export.image.toDrive({
  image: reprojectedasct,
  description: 'tetaasc',
  scale: 50,
  region: roi
});
Export.image.toDrive({
  image: reprojecteddesct,
  description: 'tetadesc',
  scale: 50,
  region: roi
});
```

Presenting the obtained data as WMS:

```
Map.addLayer(ndviS2, {min: -1, max: 1}, 'Multi-T Mean NDVI',
true);
Map.addLayer(imgasc, {min: -20, max: 0}, 'Multi-T Mean ASC',
true);
Map.addLayer(imgdesc, {min: -20, max: 0}, 'Multi-T Mean DESC',
true);
```

6.4. Python installation and processing

There is an additional version of python codes developed to run the simulations and all the processing parts for IEM and WCM algorithms. These python codes are utilized codes for developing the SMR on GEE. There are different options to install python on API of GEE to run the simulation. First option is to install GEE library on a local computer. The Earth Engine Python API is available as a Python package that can be installed locally or accessed through a Google Colab Notebook. Another option is to use the Python API package called as ee on the server side. It must be imported and initialized for each new Python session and script. To install ee library on a local machine the following scripts must be followed:

```
conda update earthengine-api
pip install earthengine-api –upgrade
import ee
```

```
ee.Authenticate()
ee.Initialize()
```

This study used a local machine to process the simulations. However, for the sake of better performance the final goal is to transfer the processing part to the servers of Google as the processing is computationally expensive which requires a huge amount processing capacity.

The following snippets are to break down the processing steps show the sequence one by one:

6.4.1. IEM simulation

To run the IEM simulation it is very important to know about the structure of database management. IEM requires six input as initial values i.e. frequency of signals in [Ghz], the incident angle in degree, two roughness parameters (rms height (s) and correlation length (l) in [cm]), and finally, the real and imaginary parts of dielectric constant values [], to carry out the simulation.

The processing starts with loading the soil moisture data as the input variable to calibrate the roughness parameters:

```
clear all
dir *.txt
filename=input('file name (without extention): ','s');
eval(['load ',filename,'.txt']);
eval(['leaf=',filename,';']);
julian=leaf(:,8);
doy=julian-(julian(1)-1);
```

The roughness parameters are given based on the certain boundary condition as described in section 3.2.1

```
% range of rms height (cm)
so=[0.01:0.01:3]';
% Range of length function (cm)
ll=[3:0.1:20]';
```

As mentioned before the obtained data from GEE come with different subsets as described below:

```

% st=2 represent 10 meters
% st=3 represent 30 meters
% st=4 represent 50 meters
% st=5 represent 70 meters
% st=6 represent 90 meters
st=4;
```

Also a comparison between the daily and instant values of soil moisture was conducted via the script below::

```
% plus + 0=daily average, or 5=instant values
xxx=8+0;
mv=leaf(:,st+xxx);
```

```
% backscatter from sentinel-1
vvm=leaf(:,st);
mv(mv<0)=nan;
```

Dobson equation was employed to convert the soil moisture values into dielectric constants as below:

```
function [ e1,e2,e,m ] = dobson(mv)

%  model parameter
sand=95;
clay=100-sand;

```

```
a0=1.993;
a1=0.002;
a2=0.015;
b0=38.086;
b1=-0.176;
b2=-0.633;
c0=10.72;
c1=1.256;
c2=1.522;

a0=-0.123;
a1=0.002;
a2=0.003;
b0=7.502;
b1=-0.058;
b2=-0.116;
c0=2.942;
c1=0.452;
c2=0.453;

e1=(a0+a1*sand+a2*clay)+(b0+b1*sand+b2*clay).*mv+(c0+c1*sand+c2*c
lay).*mv.^2;

e2=(a0+a1*sand+a2*clay)+(b0+b1*sand+b2*clay).*mv+(c0+c1*sand+c2*c
lay).*mv.^2;
e = complex(e1,e2);
end
```

The out from Dobson equation were used as an input to run the simulation as below:

```
[e1,e2]=dobson(mv);
x=length (ll);
x1=length (so);
x2=length (e1);
x3=x2*x1;
x4=x*x3;
s=so(1:x1);
l=ll(1:x);
```

Generating look up table by repeating the generated parameters for the number of observations is done by using loops as below:

```
  for j=1:length (e1)-1
     so(:,j+1)=so(:,j);
  end
  so=so';
  so=reshape(so,x3,1);
for j=1:x1-1
     e1(:,j+1)=e1(:,j);
 end
  for j=1:x1-1
     e2(:,j+1)=e2(:,j);
  end
 e1=reshape(e1,x3,1);
 e2=reshape(e2,x3,1);
 for j=1:x3-1
```

```
    ll(:,j+1)=ll(:,j);
end
ll=ll';
ll=reshape(ll,x4,1);
for j=1:x-1
    so(:,j+1)=so(:,j);
 end
    so=reshape(so,x4,1);
for j=1:x-1
    e1(:,j+1)=e1(:,j);
end

 for j=1:x-1
    e2(:,j+1)=e2(:,j);
 end

e1=reshape(e1,x4,1);
e2=reshape(e2,x4,1);

  f(1:x4)=5.405;
  f=f';
```

The incident angle was obtained from GEE and inserted and repeated for the number of observations as below:

```
teta=leaf(:,7);

for j=1:x1-1
    teta(:,j+1)=teta(:,j);
end
teta=reshape(teta,x3,1);
     for j=1:x-1
    teta(:,j+1)=teta(:,j);
     end
 teta=reshape(teta,x4,1);
```

Finally, the lookup table with all the possibilities between the roughness parameters is generated and prepared as input to run IEM simulations:

```
iemin=[f,teta,ll,so,e1,e2];
fid = fopen('iem.in','wt');
for ii = 1:size(iemin,1)
    fprintf(fid,'%g\t',iemin(ii,:));
    fprintf(fid,'\n');
end
fclose(fid);
system('iem2_Exponential.exe');
```

6.5. SMR output

From the processing that is done above a pair of roughness coefficient was selected and used as a fixed value to run IEM simulation. However, this time the soil moisture is the unknown parameter. Therefore, we created a lookup table that shows the behaviour of backscattering values based on changing the values of soil moisture as below:

```
% clear all
dir *.tif
% %insert ndvi
filename1=input('file name of ndvi (with extention): ','s');
% % insert Sentinel-1
filename2=input('file name of sentinel-1 (with extention):
','s');
% % Date is on 6 may 2018 before harvestin the winter wheat
%insert soil moisture
filename3=input('file name of soil moisture (with extention):
','s');
prompt = 'What is teta? ';
teta = input(prompt);
ndvi=imread(filename1);
[m,n]=size(ndvi);
ndvi=nanmean(ndvi);
s1=imread(filename2);
[m,n]=size(s1);
s1=reshape(s1,m*n,1);
% s1(isnan(s1))=0;
smc=imread(filename3);
so=0.26;
ll=3;
% soil moisture
mv=[0.0001:0.0001:0.71];
[e1,e2]=dobson(mv);
x=length (ll);
x1=length (so);
x2=length (e1);
x3=x2*x1;
x4=x*x3;
s=so(1:x);
l=ll(1:x);
  for j=1:length (e1)-1
     so(:,j+1)=so(:,j);
  end
  so=so';
  so=reshape(so,x3,1);
for j=1:x1-1
     e1(:,j+1)=e1(:,j);
 end

  for j=1:x1-1
     e2(:,j+1)=e2(:,j);
  end
 e1=reshape(e1,x3,1);
 e2=reshape(e2,x3,1);

 for j=1:x3-1
     ll(:,j+1)=ll(:,j);
 end
 ll=ll';
 ll=reshape(ll,x4,1);
```

```
 for j=1:x-1
     so(:,j+1)=so(:,j);
  end
     so=reshape(so,x4,1);
     for j=1:x-1
     e1(:,j+1)=e1(:,j);
 end

  for j=1:x-1
     e2(:,j+1)=e2(:,j);
  end

 e1=reshape(e1,x4,1);
 e2=reshape(e2,x4,1);

   f(1:x4)=5.405;
   f=f';

 teta(1:x4)=teta;
 teta=teta';

 iemin=[f,teta,ll,so,e1,e2];
fid = fopen('iem.in','wt');
for ii = 1:size(iemin,1)
    fprintf(fid,'%g\t',iemin(ii,:));
    fprintf(fid,'\n');
end
fclose(fid);
system('iem2_Exponential.exe');
```

6.5.1. Soil Moisture

```
readme;
vvi=10.^(vvs./10);
A=-0.2;
B=0.06;
ndvi1=[0.63];
teta=teta(1,1);
lamba=(exp(-2*B*ndvi1/cos(teta)));
sigveg=A*ndvi1*cos(teta)*(1-lamba);
bare=10*log10((10.^(s1/10)-sigveg)/lamba);

for i=1:m*n
        k=find(vvs>=(bare(i,1)-0.01)&vvs<=(bare(i,1)+0.01));
        sm=mv(k);
        sm2(i)=mean(sm);
end
```

6.5.2. RMSE/ Pearson correlation

```
sm2=reshape(sm2,m,n);
sm1=sm2(2:12,6:15);
[M,N]=size(sm1);
sm1=reshape(sm1,M*N,1);
smc=reshape(smc,M*N,1);
corel=corr(sm1,smc)
residuals=sqrt(sum((smc-sm1).^2)/M*N)
```

7. CONCLUSION

There is an expanding interest for water to inundate farming fields, particularly in warm, dry periods. Simultaneously the interest increments in different parts, including keeping up groundwater levels. It has been indicated that more water is utilized for the rural water system when the client does not have any knowledge about the soil moisture. Soil moisture-based water system hence is a way to decrease the interest for water resource management.

The objective of this study was to improve the retrieval of soil moisture for corn and wheat fields in the Twente region, the Netherlands. To carry out this study, two major sources of satellite data, including Sentinel-1 and Sentinel-2, were collected and processed via GEE to ease the data collection and processing. The soil moisture retrieval algorithm that was developed for this study is based on integrating the IEM surface scattering model with modified WCM to remove the effects of vegetation.

The spatial resolution of Sentinel-1 was aggregated to 50 meters to obtain the best spatial match with obtained soil moisture values from the LoRa network. The Roughness parameter was calibrated for corn and wheat field, separately, and validation of the Roughness parameter for corn and wheat field were conducted. The obtained roughness parameters were convincing to conduct the simulation and calculate the backscattering coefficient via IEM.

The NDVI values were calculated from Sentinel-2 level-2 product using Band 4 and band 7. The obtained NDVI values from Sentinel-2 were compared with other NDVI products, and it was concluded that NDVI derived from Sentinel-2 was the best choice to conduct this study.

The in-situ measurements of soil moisture along with Sentinel-2 observations were used as an input to calibrate A and B parameters known as crop factors for wheat and corn products. New crop factors for corn and wheat field was estimated and assessed via another set of data. The newly developed crop factors of the water cloud model improved retrieving soil moisture in corn and wheat.

The retrieved soil moisture was validated against ground measurement. The retrieved soil moisture for ascending observations in the wheat field shows 0.09 (m3/m3) RMSE error against ground measurements at a 50-meter aggregated subset. The obtained results did not show a consistent accuracy between the ascending and descending observation during the growing cycle of wheat.

On the other hand, the retrieved soil moisture in cornfield shows 0.14 and 0.13 (m3/m3) RMSE error against ground measurements for ascending and descending observations, respectively. The retrieved soil moisture uses a 90-meter aggregated subset. The obtained results show a consistent accuracy between the ascending and descending observations during the growing cycle of corn.

LIST OF REFERENCES

Attema, E. P. W., & Ulaby, F. T. (1978). Vegetation modeled as a water cloud. *Radio Science*, *13*(2), 357–364. https://doi.org/10.1029/RS013i002p00357

Aubert, M., Baghdadi, N., Zribi, M., Douaoui, A., Loumagne, C., Baup, F., … Garrigues, S. (2011). Analysis of TerraSAR-X data sensitivity to bare soil moisture, roughness, composition and soil crust. *Remote Sensing of Environment*, *115*(8), 1801–1810. https://doi.org/10.1016/j.rse.2011.02.021

Baghdadi, N., Hajj, M. El, Choker, M., Zribi, M., Bazzi, H., Vaudour, E., … Bazzi, H. (2018). Potential of Sentinel-1 Images for Estimating the Soil Roughness over Bare Agricultural Soils. *Water MDPI*, *10 (2),*(2), 131. https://doi.org/10.3390/w10020131

Baghdadi, N., Hajj, M. El, Zribi, M., & Bousbih, S. (2017). Calibration of the Water Cloud Model at C-Band for winter crop fields and grasslands. *Remote Sensing*, *9*(9), 1–13. https://doi.org/10.3390/rs9090969

Barrett, B. W., Dwyer, E., & Whelan, P. (2009). Soil moisture retrieval from active spaceborne microwave observations: An evaluation of current techniques. *Remote Sensing*, *1*(3), 210–242. https://doi.org/10.3390/rs1030210

Benninga, H.-J. F., van der Velde, R., & Su, Z. (2019). Impacts of Radiometric Uncertainty and Weather-Related Surface Conditions on Soil Moisture Retrievals with Sentinel-1. *Remote Sensing*, *11*(17), 2025. https://doi.org/10.3390/rs11172025

Bindlish, R. ., Jackson, T. ., Sun, R. ., Cosh, M. ., Yueh, S. ., & Dinardo, S. (2009). Combined passive and active microwave observations of soil moisture during CLASIC. *IEEE Geosci. Remote Sens. Lett.*, *6*(4), 644–648.

Bryant, R., Moran, M. S., Thoma, D. P., Holifield Collins, C. D., Skirvin, S., Rahman, M., … González Dugo, M. P. (2007). Measuring surface roughness height to parameterize radar backscatter models for retrieval of surface soil moisture. *IEEE Trans. Geosci. Remote Sens., 4*(1), 137–141.

CBS. (2016). Compendium voor de Leefomgeving. Retrieved June 20, 2020, from www.clo.nl

Choker, M., Baghdadi, N., Zribi, M., El Hajj, M., Paloscia, S., Verhoest, N. E. C., … Mattia, F. (2017). Evaluation of the Oh, Dubois and IEM backscatter models using a large dataset of SAR data and experimental soil measurements. *Water (Switzerland)*, *9*(1). https://doi.org/10.3390/w9010038

Cui, C., Xu, J., Zeng, J., Chen, K. S., Bai, X., Lu, H., … Zhao, T. (2018). Soil moisture mapping from satellites: An intercomparison of SMAP, SMOS, FY3B, AMSR2, and ESA CCI over two dense network regions at different spatial scales. *Remote Sensing*, *10*(1). https://doi.org/10.3390/rs10010033

Dam, R. L. van, Borchers, B., Hendrickx, J. M. H., & Harmon, R. S. (2003). Effects of soil water content and texture on radar and infrared landminesensors: implications for sensor fusion. *Proc. of the Internat. Conf. on Requirements and Technologies for the Detection,Removal, and Neutralization of Landmines and UXO*, *1*, 107–114.

Darvishzadeh, R., Atzberger, C., Skidmore, A., & Schlerf, M. (2011). Mapping grassland leaf area index with airborne hyperspectral imagery: A comparison study of statistical approaches and inversion of radiative transfer models. *ISPRS Journal of Photogrammetry and Remote Sensing*, *66*(6), 894–906. https://doi.org/10.1016/j.isprsjprs.2011.09.013

Decagon. (2016). *5TM Sensor Integrator Guide* (Vol. 3).

Dobson, M. C. M., Ulaby, F. F. T., Hallikainen, M. M. T., & El-rayes, M. A. M. (1985). Microwave

Dielectric Behavior of Wet Soil-Part II: Dielectric Mixing Models. *IEEE Transactions on Geoscience and Remote Sensing*, *GE-23*(1), 35–46.

Dubois, P. C. ., Van Zyl, J. ., & Engman, T. (1995). Measuring soil moisture with imaging radars. *IEEE Trans. Geosci. and Remote Sensing*, *33*, 915–926. Retrieved from https://ieeexplore.ieee.org/document/406677

Entekhabi, D., Yueh, Si., O'Neil, P. E., Kellogg, K. H., Allen, A., Bindlish, R., & Administration, N. A. and S. (2014). SMAP Handbook. *Mapping Soil Moisture and Freeze/Thaw from Space*, 192.

FAO. (2018). *Using remote sensing in support of solutions to reduce agricultural water productivity gaps. Database methodology: Level 2 data. WaPOR Version 1* (Vol. 1). Rome.

Feng, A., Zhou, J., Vories, E., & Sudduth, K. A. (2020). Evaluation of cotton emergence using uav-based narrow-band spectral imagery with customized image alignment and stitching algorithms. *Remote Sensing*, *12*(11). https://doi.org/10.3390/rs12111764

Fung, A. K., Li, Z., & Chen, K. S. (1992). Backscattering from a Randomly Rough Dielectric Surface. *IEEE Transactions on Geoscience and Remote Sensing*. https://doi.org/10.1109/36.134085

Gorelick, N., Hancher, M., Dixon, M., Ilyushchenko, S., Thau, D., & Moore, R. (2017). Google Earth Engine: Planetary-scale geospatial analysis for everyone. *Remote Sensing of Environment*, *202*, 18–27. https://doi.org/10.1016/j.rse.2017.06.031

Gorrab, A., Zribi, M., Baghdadi, N., Mougenot, B., Fanise, P., & Chabaane, Z. L. (2015). Retrieval of both soil moisture and texture using TerraSAR-X images. *Remote Sensing*, *7*(8), 10098–10116. https://doi.org/10.3390/rs70810098

Hajj, M. El, Baghdadi, N., Zribi, M., & Bazzi, H. (2017). Synergic use of Sentinel-1 and Sentinel-2 images for operational soil moisture mapping at high spatial resolution over agricultural areas. *Remote Sensing*, *9*(12). https://doi.org/10.3390/rs9121292

Hollstein, A., Segl, K., Guanter, L., Brell, M., & Enesco, M. (2016). Ready-to-use methods for the detection of clouds, cirrus, snow, shadow, water and clear sky pixels in Sentinel-2 MSI images. *Remote Sensing*, *8*(8), 1–18. https://doi.org/10.3390/rs8080666

Hosseini, M., McNairn, H., Merzouki, A., & Pacheco, A. (2015). Estimation of Leaf Area Index (LAI) in corn and soybeans using multi-polarization C- and L-band radar data. *Remote Sensing of Environment*, *170*, 77–89. https://doi.org/10.1016/j.rse.2015.09.002

Joseph, A. T., van der Velde, R., O'Neill, P. E., Lang, R., & Gish, T. (2010). Effects of corn on C- and L-band radar backscatter: A correction method for soil moisture retrieval. *Remote Sensing of Environment*, *114*(11), 2417–2430. https://doi.org/10.1016/j.rse.2010.05.017

Kirimi, F., Kuria, D. N., Thonfeld, F., Amler, E., Mubea, K., Misana, S., & Menz, G. (2016). Influence of Vegetation Cover on the Oh Soil Moisture Retrieval Model: A Case Study of the Malinda Wetland, Tanzania. *Advances in Remote Sensing*, *05*(01), 28–42. https://doi.org/10.4236/ars.2016.51003

Kornelsen, K. C., & Coulibaly, P. (2013). Advances in soil moisture retrieval from synthetic aperture radar and hydrological applications. *Journal of Hydrology*, *476*, 460–489. https://doi.org/10.1016/j.jhydrol.2012.10.044

Kumar, D., Rao, S., & Sharma, J. R. (2013). Radar Vegetation Index as an Alternative to NDVI for Monitoring of Soyabean and Cotton. *Proceedings of the XXXIII INCA International Congress (Indian Cartographer), 19-21 September, 2013, Jodhpur, India,* (September 2013), 91–96.

Lievens, H., Vernieuwe, H., Álvarez-Mozos, J., Baets, B., & Verhoest, N. (2009). Error in radar-derived soil moisture due to roughness parameterization: An analysis based on synthetical surface profiles. *Sensors MDPI*, *9*(2), 1067–1093. https://doi.org/10.3390/s90201067

Martínez-Fernández, J., González-Zamora, A., Sánchez, N., Gumuzzio, A., & Herrero-Jiménez, C. M. (2016). Satellite soil moisture for agricultural drought monitoring: Assessment of the SMOS derived Soil Water Deficit Index. *Remote Sensing of Environment*, *177*, 277–286. https://doi.org/10.1016/j.rse.2016.02.064

Mattia, F., Toan, T. Le, Picard, G., Posa, F. I., D'Alessio, A., Notarnicola, C., … Pasquariello, G. (2003). Multitemporal c-band radar measurements on wheat fields. *IEEE Transactions on Geoscience and Remote Sensing*, *41*(7), 1551–1560. https://doi.org/10.1109/TGRS.2003.813531

Mironov, V. L., Kosolapova, L. G., & Fomin, S. V. (2009). Physically and mineralogically based spectroscopic dielectric model for moist soils. *IEEE Transactions on Geoscience and Remote Sensing*, *47*(7), 2059–2070. https://doi.org/10.1109/TGRS.2008.2011631

Nieber, J. L. (1982). Finite Element Analysis of Soil Moisture Flow and Moisture Stress in a Dessicating Soil. In K. P. Holz, U. Meissner, W. Zielke, C. A. Brebbia, G. Pinder, & W. Gray (Eds.), *Finite Elements in Water Resources* (pp. 717–726). Berlin, Heidelberg: Springer Berlin Heidelberg.

Nyamu, P. W. (2019). *Assessment of satellite based soil moisture products at various spatial scales for dry-down cycles analysis*. Faculty of Geo-Information Science and Earth Observation of the University of Twente.

Oh, Y., Sarabandi, K., & Ulaby, F. T. (1994). An inversion algorithm for retrieving soil moisture and surface roughness from polarimetric radar observations. In *Geoscience Remote Sensing Symp.*

Oh, Yisok;, Sarabandi, K., & Ulaby, F. (1992). An empirical model and an inversion technique for radar scattering from bare soil surfaces. *IEEE Transactions on Geoscience and Remote Sensing*, *30*(2), 370–381.

Picard, G., Le Toan, T., & Mattia, F. (2003). Understanding C-band radar backscatter from wheat canopy using a multiple-scattering coherent model. *IEEE Transactions on Geoscience and Remote Sensing*, *41*(7 PART I), 1583–1591. https://doi.org/10.1109/TGRS.2003.813353

Pierdicca, N., Pulvirenti, L., & Bignami, C. (2010). Soil moisture estimation over vegetated terrains using multitemporal remote sensing data. *Remote Sensing of Environment*, *114*(2), 440–448. https://doi.org/10.1016/j.rse.2009.10.001

Rodriguez-Alvarez, N., Bosch-Lluis, X., Camps, A., Aguasca, A., Vall-Llossera, M., Valencia, E., … Park, H. (2011). Review of crop growth and soil moisture monitoring from a ground-based instrument implementing the Interference Pattern GNSS-R Technique. *Radio Science*, *46*(5), 1–11. https://doi.org/10.1029/2011RS004680

Rouse, J. W., R. H., Haas, J. A., Schell, & Deering, D. W. (1973). Rouse, J. W., R. H. Haas, J. A. Schell, and D. W. Deering (1973). ,. In *Monitoring vegetation systems in the Great Plains with ERTS, Third ERTS Symposium* (pp. 309–317). Texas: NASA SP-351 I.

Sazib, N., Mladenova, I., & Bolten, J. (2018). Leveraging the google earth engine for drought assessment using global soil moisture data. *Remote Sensing*, *10*(8). https://doi.org/10.3390/rs10081265

Srivastava, H. S., Patel, P., & Navalgund, R. (2006). Incorporating soil texture in soil moisture estimation from extended low-1 beam mode RADARSAT-1 SAR data. *International Journal of Remote Sensing*, *27*(12), 2587–2598. https://doi.org/10.1080/01431160500497838

Ulaby, F., & Long, D. (2014). Microwave Radar and Radiometric Remote Sensing. *Microwave Radar and Radiometric Remote Sensing*, (March 2016). https://doi.org/10.3998/0472119356

Veci, L. (2015). Sentinel-1 Toolbox Interferometry Tutorial. *Array Systems Computing Inc*, (March), 1–20.

Retrieved from http://www.ggki.hu/banyai/S1TBX/S1TBX Stripmap Interferometry with Sentinel-1 Tutorial.pdf

Verhoest, N. E. C., De Baets, B., Mattia, F., Satalino, G., Lucau, C., & Defourny, P. (2007). A possibilistic approach to soil moisture retrieval from ERS synthetic aperture radar backscattering under soil roughness uncertainty. *Water Resources Research*. https://doi.org/10.1029/2006WR005295

Verhoest, N. E. C., Lievens, H., Wagner, W., Álvarez-Mozos, J., Moran, M. S., & Mattia, F. (2008). On the soil roughness parameterization problem in soil moisture retrieval of bare surfaces from synthetic aperture radar. *IEEE Trans. Geosci. Remote Sens.*, *8*(7), 4213–4248.

Zhang, F., & Zhou, G. (2019). Estimation of vegetation water content using hyperspectral vegetation indices: A comparison of crop water indicators in response to water stress treatments for summer maize. *BMC Ecology*, *19*(1), 1–12. https://doi.org/10.1186/s12898-019-0233-0

Zhang, X., Tang, X., Gao, X., & Zhao, H. (2018). Multitemporal Soil Moisture Retrieval over Bare Agricultural Areas by Means of Alpha Model with Multisensor SAR Data. *Advances in Meteorology*, *2018*. https://doi.org/10.1155/2018/7914581